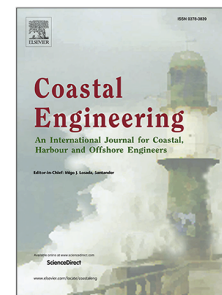


# Journal Pre-proof

Full-scale tsunami-induced scour around a circular pile with three-dimensional seepage

Zhengyu Hu, Yuzhu Pearl Li



PII: S0378-3839(24)00224-2

DOI: <https://doi.org/10.1016/j.coastaleng.2024.104676>

Reference: CENG 104676

To appear in: *Coastal Engineering*

Received date: 13 August 2024

Revised date: 13 November 2024

Accepted date: 29 November 2024

Please cite this article as: Z. Hu and Y.P. Li, Full-scale tsunami-induced scour around a circular pile with three-dimensional seepage. *Coastal Engineering* (2024), doi: <https://doi.org/10.1016/j.coastaleng.2024.104676>.

This is a PDF file of an article that has undergone enhancements after acceptance, such as the addition of a cover page and metadata, and formatting for readability, but it is not yet the definitive version of record. This version will undergo additional copyediting, typesetting and review before it is published in its final form, but we are providing this version to give early visibility of the article. Please note that, during the production process, errors may be discovered which could affect the content, and all legal disclaimers that apply to the journal pertain.

© 2024 Published by Elsevier B.V.

# Full-scale tsunami-induced scour around a circular pile with three-dimensional seepage

Zhengyu Hu<sup>a</sup>, Yuzhu Pearl Li<sup>a,\*</sup>

<sup>a</sup>*National University of Singapore, Department of Civil and Environmental Engineering, Singapore*

## Abstract

Seepage flows induced by geophysical tsunamis play a significant role in the tsunami boundary layer dynamics and associated sediment mobility. However, its impact on sediment transport and seabed morphodynamics in the presence of coastal structures remains unclear. In this study, we conduct rigid-bed and morphological simulations to investigate the role of seepage response in full-scale tsunami-induced flow features and sediment transport around a circular pile. The expressions for the onset threshold of sediment transport and the bed load motions are derived considering both bed-slope modifications and three-dimensional seepage forces, which are implemented in the coupled hydrodynamic, morphological, and soil models. The rigid-bed simulations demonstrate that the seabed suction response to the elevation wave can reduce the bed shear stress amplification underneath the contraction of streamlines alongside the pile and lee-wake vortices. The seabed injection response to the depression wave increases the stress amplification. It advances the position of boundary layer separation over the height of the pile, which further changes the lee-wake vortices. Note that the size of the horseshoe vortex and the upward-directed pressure gradient within it are less affected by the seepage flows. In morphological simulations, suspended load transport dominates the scour around the pile. Seabed suction during the elevation wave can slightly reduce the sediment transport rate, decreasing the scour depth, especially at the pile side. Seabed injection during the elevation wave causes exacerbated suspended load transport, leading to a more rapid and severe scour at the back of the pile. This study advances the un-

\*Corresponding author

Email address: pearl.li@nus.edu.sg (Yuzhu Pearl Li)

derstanding of seepage effects on tsunami-induced sediment transport and scour around a monopile foundation.

*Keywords:* Tsunamis, Seepage response, Scour, Pile, Sediment transport

## 1. Introduction

2 Tsunamis can cause devastating impacts when they reach coastlines, re-  
 3 sulting in widespread flooding, destruction of coastal infrastructure, and loss  
 4 of life (Lynett et al., 2022; Robbe-Saule et al., 2021; Sarlin et al., 2021). The  
 5 destructive potential of tsunamis extends beyond the immediate impact of  
 6 the waves. Altered seabed topography, changes in sediment composition, and  
 7 the redistribution of nutrients can pose threats to infrastructure and impact  
 8 coastal ecosystems (Dawson and Shi, 2000; Mori et al., 2011; Apotsos et al.,  
 9 2011; Jayaratne et al., 2016; McGovern et al., 2019). Tsunami field surveys  
 10 from the 1992 Nicaragua tsunami to the recent 2022 Tonga tsunami have  
 11 provided valuable insights into the scouring effects on coastal structures and  
 12 the associated sediment transport dynamics (Satake et al., 1993; Fritz et al.,  
 13 2007; Lacy et al., 2012; Yeh et al., 2013; Borrero et al., 2023). Understanding  
 14 these processes is crucial for assessing tsunamis' long-term ecological and ge-  
 15 ological impacts, informing disaster management strategies, and promoting  
 16 resilient coastal development in vulnerable regions.

17 Monopiles are widely used in marine environments for offshore wind  
 18 farms, oil/gas platforms, and bridge foundations (Gupta and Basu, 2020;  
 19 Zou et al., 2021; Guan et al., 2022). While there have been numerous studies  
 20 on scour around piles subjected to waves (Sumer et al., 1992; Sumer and Fredsøe,  
 21 2002; Baykal et al., 2017; Chen et al., 2022; Zhang et al., 2023),  
 22 tidal currents (Roulund et al., 2005; Zhao and Cheng, 2008; Zhao et al., 2010;  
 23 Baykal et al., 2015; Whitehouse and Stroescu, 2023), and combined waves  
 24 and current (Sumer and Fredsøe, 2001; Sumer et al., 2013; Qi and Gao, 2014;  
 25 Chen and Li, 2018; Larsen and Fuhrman, 2023) in past decades, the potential  
 26 scour induced by the tsunami attack has received relatively little specific at-  
 27 tention. Tsunamis are expected to have different scour mechanics from these  
 28 conventional ocean loads. From the hydrodynamic perspective, tsunamis are  
 29 characterized by long waves, typically with periods spanning from minutes to  
 30 hours and wavelengths extending over hundreds of kilometers (Carrier et al.,  
 31 2003; Madsen et al., 2008; Chan and Liu, 2012; Liu and Higuera, 2022). The  
 32 tsunami propagation and inundation have been extensively investigated (Sug-

awara et al., 2014; Larsen and Fuhrman, 2019a; Omira et al., 2022; Ren et al., 2023). The studies on the associated boundary layer dynamics are limited but significant for assessing the interaction with the seabed, i.e., sediment transport and morphological process. Williams and Fuhrman (2016) numerically simulated the transient wave boundary layers at full-tsunami scales using a one-dimensional vertical (1DV) Reynolds-averaged Navier-Stokes (RANS) model, which suggests that the boundary layers underneath tsunamis exhibit characteristics akin to currents, owing to their prolonged duration, while also retaining wave-like attributes, as their thickness may not extend across the entire water depth. This aligns with field measurements recorded in northern Monterey Bay during the 2010 Chile tsunami arrival (Lacy et al., 2012), as well as computational fluid dynamics (CFD) simulations conducted on full-scale tsunamis approaching various constant sloped areas (Larsen and Fuhrman, 2019b).

There are limited studies on the tsunami-induced scour around offshore and coastal structures. Wilson et al. (2012) compared the video, bathymetry, and sediment data from harbors in California (USA) before and after the 2011 Tohoku tsunami. They showed significant scour and deposition within the harbors, which could contribute to the weakening foundations and long-term usability problems. Additionally, Bricker et al. (2012) conducted field measurements on the scour depth on the landward side of seawalls and foundation footings induced by the 2011 Tohoku tsunami. Chen et al. (2013) investigated tsunami-induced scour at coastal roadways through experimental studies. Larsen et al. (2017, 2018) numerically and experimentally investigated the tsunami-induced scour around a monopile structure using the standard shear stress descriptions, where the tsunami flow is represented as a time-varying current, and the free-stream velocity is given by either a sinusoidal wave or a single wave (elongated soliton). However, Tonkin et al. (2003) found that the standard shear stress model cannot qualitatively explain the rapid scour at the back of the cylinder under low flow velocity at the end of tsunami draw-down from a large-scale experiment. They showed that the development of pore-pressure gradients in the underlying soil associated with rapid drops in water levels buoys up the superficial sediment, which decreases the onset threshold of the sediment motion. When the pore-pressure gradient exceeds the buoyant weight of the sediment, the effective stress between sediment grains could vanish to form momentary liquefaction, making the sediment readily scoured (Sumer and Fredsøe, 2002; Sumer, 2014; Qi and Gao, 2018; Li et al., 2018, 2020a). The effect of the increased pore-pressure

gradient on the tsunami scour process was studied by Nakamura et al. (2008) for a land-based square structure and by Hu et al. (2024) for a submarine pipeline. The tsunami-induced momentary liquefaction was detected in the large-scale experiments of Yoshii et al. (2017, 2018), analytical and numerical solutions (Liu et al., 2007; Tong and Liu, 2022), and the collapse processes of a quay wall in Konakano, Japan, under no ground shaking and low flow velocity during the draw-down period of the 1960 Chilean tsunami, as reported by Yeh and Mason (2014). Understanding the effect of pore-pressure gradients is crucial for accurately estimating tsunami-induced scour.

Recent studies have attempted to reveal the effect of pore-pressure gradients on sediment transport. The incipient motion threshold for sediment particles on a flatbed subjected to the vertical (Guo et al., 2019), two-dimensional (Zhai et al., 2021a; Wang et al., 2024), and three-dimensional seepage forces (Zhai et al., 2021b) were modified from the classic Shields parameter description. The bed-slope modifications on the critical Shields parameter and bed load transportation were further considered in the presence of vertical seepage forces (Cheng and Chiew, 1999; Li et al., 2020a; Hu et al., 2024). However, the general expression considering both bed-slope modifications and three-dimensional seepage forces has not yet been proposed. In addition to seepage forces, the seepage velocities induced by pore-pressure gradients could, in turn, significantly affect the profiles of the near-bed flow velocity and bed shear stresses (Cheng and Chiew, 1998; Chen and Chiew, 2004; Dey and Nath, 2010; Sharma and Kumar, 2017; Li et al., 2020a; Taye et al., 2023). Hu et al. (2024) showed the competing seepage effects on the onset threshold of sediment transport and the bed shear stress, which results in not necessarily increased bed load transport during the tsunami draw-down. However, most previous models addressing seepage effects on sediment transport have overlooked these impacts. The bed shear stress influenced by seepage velocities was not resolved due to the one-way coupling of the model (Guo et al., 2019; Zhai et al., 2021a; Zhai and Jeng, 2024). Incorporating the two-way coupling of wave pressure and soil response such as Zhai and Jeng (2022) and Ye et al. (2024) into the sediment transport and seabed morphological model can better characterize the role of seepage effects on scour. Sui et al. (2024) investigated seabed response and liquefaction around monopile in the context of short waves. The pre-specified scour hole reduces pore pressure and creates a more uniform liquefaction depth around the monopile, which intensifies with higher soil saturation but varies with permeability. The role of seepage response on the flow features and scour

around monopiles induced by the tsunami attack has not been previously studied, either experimentally or numerically. In scaled flume experiments, the pore-pressure gradients induced by waves in the surficial seabed are usually much lower than the buoyant weight of the sediment (Qi and Gao, 2014). Moreover, replicating tsunami waves experimentally is indeed challenging due to their prolonged duration. Consequently, it is hard to directly observe the seepage effects on tsunami scour in a laboratory experiment.

In the present study, we conduct full-scale rigid-bed and morphological simulations to investigate the role of seepage response in tsunami-induced flow features and scour around a circular pile. The remainder of the paper is organized as follows. Section 2 presents the onset threshold of sediment transport and the bed load transportation for the particle on a sloping bed subjected to the three-dimensional seepage forces. These are implemented into the coupled hydrodynamic, morphological, and soil models. The model is then validated against the laboratory experiments of a turbulent boundary layer subjected to seepage velocities and tsunami-induced scour around a monopile. Section 3 describes the used full-scale tsunami signal and the corresponding seepage response. Section 4 discusses the main tsunami flow features around a circular pile with and without considering the seepage effects. Section 5 presents the seepage effects on the evolution of tsunami-induced scour. Finally, conclusions are drawn in Section 6.

## 2. Models and methodologies

In this section, we first derive the onset threshold of sediment transport and the bed load transportation for a particle on a sloping bed subjected to the three-dimensional seepage forces in Sections 2.1 and 2.2. We then present the fully coupled hydrodynamic, morphological, and soil models with further consideration of the dynamic seepage response in Section 2.3. Furthermore, we validate the model against laboratory experiments in Section 2.4. Finally, we show the model setup and boundary conditions for simulating the sediment transport and morphological processes around a circular pile subjected to the tsunami waves in Section 2.5.

### 2.1. Onset threshold of sediment transport

For flow over a bed composed of cohesionless grains (see Fig. 1), the driving force on a non-moving spherical sediment particle consists of the flow-induced drag force  $F_D$  in the flow direction and lift force  $F_L$  in excess

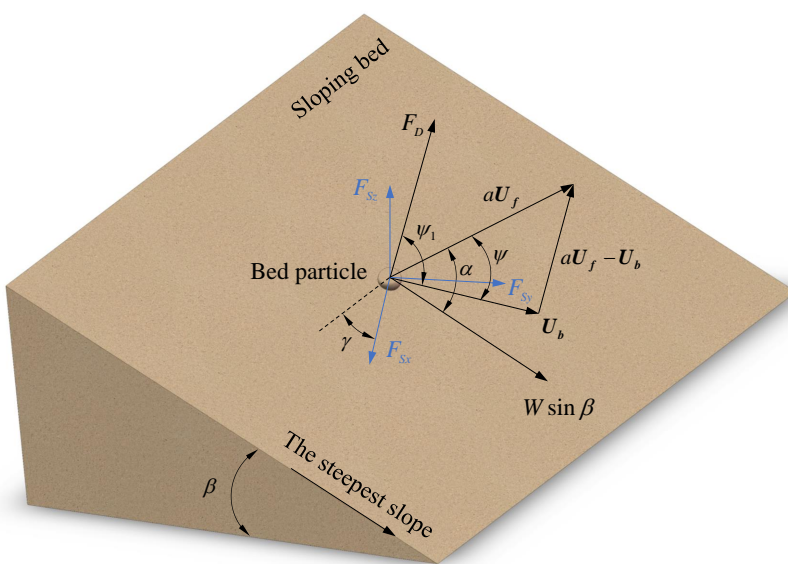


**Fig. 1.** Force balance on a single moving sediment particle on a sloping bed.

of the natural buoyancy. Since the lift force has a similar expression as the drag force, the driving force can be given in the following form (Fredsøe and Deigaard, 1992, pp. 201–202)

$$F_D = \frac{1}{2} \rho C_D \frac{\pi}{4} d^2 (a U_f)^2, \quad (1)$$

where  $\rho$  is the density of fluid,  $C_D$  stands for a drag (and lift) coefficient,  $d$  is the median diameter of the particle,  $U_f$  is the friction velocity, and  $a$  is an empirical constant, taken as  $a = 10$  (Engelund and Fredsøe, 1976; Roulund et al., 2005). The three-dimensional seepage force  $F_S = (F_{Sx}, F_{Sy}, F_{Sz})$  in the Cartesian coordinate system is induced by the pore-pressure gradient at the bed surface, expressed as

$$F_S = \frac{i \rho g \pi d^3}{6(1-n)}, \quad (2)$$

where  $i = (i_x, i_y, i_z)$  is the hydraulic gradient at the surficial bed,  $g$  is the gravitational acceleration, and  $n$  is the porosity of the sediment particles

<sup>155</sup> (Cheng and Chiew, 1998). The submerged weight of the particle is given by

$$W = \frac{(s - 1) \rho g \pi d^3}{6}, \quad (3)$$

<sup>156</sup> where  $s$  denotes the specific gravity. The stabilizing force is the frictional  
<sup>157</sup> force acting on a particle at rest. The threshold of the incipient sediment  
<sup>158</sup> motion on a sloping bed is attained when the driving force on the particle is  
<sup>159</sup> about to exceed the stabilizing force

$$\begin{aligned} & (F_{Dc} \sin \alpha - F_{Sx} \cos \gamma + F_{Sy} \sin \gamma)^2 \\ & + [F_{Dc} \cos \alpha + (W - F_{Sz}) \sin \beta + (F_{Sx} \sin \gamma + F_{sy} \cos \gamma) \cos \beta]^2 \quad (4) \\ & = \mu_s^2 [(W - F_{Sz}) \cos \beta - (F_{Sx} \sin \gamma + F_{Sy} \cos \gamma) \sin \beta]^2, \end{aligned}$$

<sup>160</sup> where  $F_{Dc}$  is the critical drag force,  $\beta$  is the angle of the sloping bed, i.e., the  
<sup>161</sup> angle between the steepest slope and horizontal plane,  $\alpha$  is the angle between  
<sup>162</sup> the flow velocity vector and the direction of the steepest bed slope,  $\gamma$  is  
<sup>163</sup> the angle between  $F_{Sx}$  and the transverse direction of the bed slope,  $\mu_s =$   
<sup>164</sup>  $\tan \beta_r$  is the static friction coefficient for the sediment, and  $\beta_r$  is the angle  
<sup>165</sup> of repose. Assuming that the seepage flow marginally influences the static  
<sup>166</sup> friction coefficient of sediment particles (Zhai and Jeng, 2024), the force  
<sup>167</sup> balance determines the dimensionless form of the critical bed shear stress,  
<sup>168</sup> critical Shields parameter  $\theta_c$

$$\theta_c = \frac{U_{fc}^2}{(s - 1) gd} = \frac{\theta_{co,i=0}}{\mu_s i_c} \left[ A \sin \alpha - B \cos \alpha + \sqrt{(A \sin \alpha - B \cos \alpha)^2 - (A^2 + B^2 - C^2)} \right], \quad (5)$$

<sup>169</sup> where  $U_{fc}$  is the critical friction velocity and  $i_c = (s - 1)(1 - n)$  is the critical  
<sup>170</sup> hydraulic gradient to cause fluidization of a bed, which is determined by the  
<sup>171</sup> specific gravity and porosity of sediment grains.  $\theta_{co,i=0} = 4\mu_s/3a^2C_D$  is the  
<sup>172</sup> critical Shields parameter on a flatbed without seepage flows, which can be  
<sup>173</sup> obtained from the classic Shields diagram (Fredsøe and Deigaard, 1992, pp.

<sup>174</sup> 201–203). The coefficients are given by

$$\left. \begin{aligned} A &= i_x \cos \gamma - i_y \sin \gamma; \\ B &= (i_c - i_z) \sin \beta + (i_x \sin \gamma + i_y \cos \gamma) \cos \beta; \\ C &= \mu_s [(i_c - i_z) \cos \beta - (i_x \sin \gamma + i_y \cos \gamma) \sin \beta]. \end{aligned} \right\} \quad (6)$$

<sup>175</sup> When only the vertical seepage force is considered, i.e.,  $i_x = 0$  and  $i_y = 0$ ,  
<sup>176</sup> the critical Shields parameter can be reduced to the expression proposed by  
<sup>177</sup> Hu et al. (2024)

$$\theta_c = \left(1 - \frac{i_z}{i_c}\right) \left( \cos \beta \sqrt{1 - \frac{\sin^2 \alpha \tan^2 \beta}{\mu_s^2}} - \frac{\cos \alpha \sin \beta}{\mu_s} \right) \theta_{co,i=0}. \quad (7)$$

<sup>178</sup>

## <sup>179</sup> 2.2. Bed load transportation

<sup>180</sup> We extend the bed load transport formulation of Roulund et al. (2005),  
<sup>181</sup> who extended the well-known transport formulation of Engelund and Fredsøe  
<sup>182</sup> (1976) to include three-dimensional effects as well as bed-slope modifica-  
<sup>183</sup> tions, to consider an additional three-dimensional seepage force induced by  
<sup>184</sup> the pore-pressure gradient in the soil. The bed load formula considers the  
<sup>185</sup> equilibrium of forces acting on a bed load particle, containing the agitating  
<sup>186</sup> and the stabilizing forces. When the bed load particles are moving with a  
<sup>187</sup> mean transport velocity  $U_b$  shown in Fig. 1, the agitating force due to the  
<sup>188</sup> streamwise flow is expressed by (Fredsøe and Deigaard, 1992, p. 210)

$$F_D = \frac{1}{2} \rho C_D \frac{\pi}{4} d^2 U_r^2, \quad (8)$$

<sup>189</sup> where  $U_r$  is the relative velocity between the flow and the particle

$$\mathbf{U}_r = a \mathbf{U}_f - \mathbf{U}_b, \quad (9)$$

<sup>190</sup> and  $C_D$  can be obtained from the force balance for a bed load particle on a  
<sup>191</sup> horizontal bed under the critical velocity, which is further modified according

<sup>192</sup> to the experimental data (Fredsøe and Deigaard, 1992, p. 211)

$$C_D = \frac{4\mu_d}{3a^2 (\frac{1}{2}\theta_{co})}, \quad (10)$$

<sup>193</sup> where  $\mu_d$  represents the dynamic friction coefficient,  $\frac{1}{2}\theta_{co}$  was suggested by  
<sup>194</sup> Fernandez Luque and Van Beek (1976) from their experimental observations.

<sup>195</sup> We consider the two components of the equation of the particle motion  
<sup>196</sup> influenced by the three-dimensional seepage force. Assuming that the par-  
<sup>197</sup> ticles move at a constant velocity on average  $U_b$ , the equation of motion in  
<sup>198</sup> the direction of the particle motion is:

$$\begin{aligned} F_D \cos \psi_1 + [(W - F_{Sz}) \sin \beta + (F_{Sx} \sin \gamma + F_{Sy} \cos \gamma) \cos \beta] \cos(\alpha - \psi) \\ - (F_{Sx} \cos \gamma - F_{Sy} \sin \gamma) \sin(\alpha - \psi) \\ - \mu_d [(W - F_{Sz}) \cos \beta - (F_{Sx} \sin \gamma + F_{Sy} \cos \gamma) \sin \beta] = 0. \end{aligned} \quad (11)$$

<sup>199</sup> The equation of motion in the direction perpendicular to  $U_b$ , on the other  
<sup>200</sup> hand, reads:

$$\begin{aligned} F_D \sin \psi_1 - [(W - F_{Sz}) \sin \beta + (F_{Sx} \sin \gamma + F_{Sy} \cos \gamma) \cos \beta] \sin(\alpha - \psi) \\ - (F_{Sx} \cos \gamma - F_{Sy} \sin \gamma) \cos(\alpha - \psi) = 0. \end{aligned} \quad (12)$$

<sup>201</sup> There are also the following geometric relations from Fig. 1

$$U_r \sin \psi_1 - aU_f \sin \psi = 0, \quad (13)$$

<sup>202</sup> and

$$U_r \cos \psi_1 - aU_f \cos \psi + U_b = 0. \quad (14)$$

<sup>203</sup> Eqs. (11)–(14) are to be solved for the four unknowns, namely  $U_b$ ,  $U_r$ ,  $\psi$ , and

<sup>204</sup>  $\psi_1$ . The Newton–Raphson technique has solved these equations in full form.

<sup>205</sup> Once mean particle velocity  $U_b$  is determined, the rate of bed load transport

<sup>206</sup>  $q_b$  can be determined by (Fredsøe and Deigaard, 1992, p. 211)

$$q_b = \frac{\pi}{6} d^3 \frac{p_{EF}}{d^2} U_b, \quad (15)$$

<sup>207</sup> where  $p_{EF}$  is the percentage of the topmost particles in motion, expressed by

<sup>208</sup> (Fredsøe and Deigaard, 1992, p. 213)

$$p_{EF} = \left[ 1 + \left( \frac{\pi \mu_d}{6(\theta - \theta_c)} \right)^4 \right]^{-1/4}, \quad (16)$$

<sup>209</sup> where the dimensionless form of the bed shear stress, Shields parameter  $\theta$ , is  
<sup>210</sup> given by

$$\theta = \frac{U_f^2}{(s-1)gd}. \quad (17)$$

<sup>211</sup> *2.3. Hydrodynamic, morphological, and soil models*

<sup>212</sup> The numerical model used in this study integrates the fully coupled  
<sup>213</sup> hydrodynamic and morphological CFD framework introduced by Jacobsen  
<sup>214</sup> (2011) and Jacobsen et al. (2014), with the additional incorporation of the  
<sup>215</sup> dynamic seepage response obtained by the anisotropic Biot's consolidation  
<sup>216</sup> model (Biot, 1941).

<sup>217</sup> The hydrodynamic model solves the incompressible three-dimensional  
<sup>218</sup> RANS equations within a Cartesian coordinate system. The closure is achieved  
<sup>219</sup> using the two-equation  $k-\omega$  turbulence model proposed by Wilcox (2006,  
<sup>220</sup> 2008), where  $k$  represents turbulent kinetic energy, and  $\omega$  denotes specific  
<sup>221</sup> turbulent dissipation rate. The morphological model addresses both bed  
<sup>222</sup> load and suspended load transport. Bed load transport follows the method  
<sup>223</sup> described in Section 2.1 and 2.2. Expressions for critical bed shear stress  
<sup>224</sup> and bed load transport are adapted to incorporate the influence of three-  
<sup>225</sup> dimensional seepage forces and bed-slope modifications. The suspended sedi-  
<sup>226</sup> ment model is based on a turbulent-diffusion equation (Fredsøe and Deigaard,  
<sup>227</sup> 1992, p. 238). The evolution of seabed morphology, represented by bed eleva-  
<sup>228</sup> tion, is governed by a sediment continuity (Exner) equation. A physics-based  
<sup>229</sup> sand slide model (Roulund et al., 2005) is employed to ensure that the local  
<sup>230</sup> bed angle does not surpass the angle of repose. The evolution of bed mor-  
<sup>231</sup> phology is based on the instantaneous sediment transport fields. Note that  
<sup>232</sup> the model does not rely on averaged morphological rates over a specific time  
<sup>233</sup> frame or any other temporal scale. Therefore, morphological and hydrody-  
<sup>234</sup> namic times are equivalent, i.e., the morphological and hydrodynamic models  
<sup>235</sup> are fully coupled. For comprehensive understanding, readers are directed to  
<sup>236</sup> Fuhrman et al. (2014) for further elucidation. The seepage response is based  
<sup>237</sup> on the soil model developed by Li et al. (2020c) who employed the classical

<sup>238</sup> Biot's consolidation equations (Biot, 1941) to simulate the interaction be-  
<sup>239</sup> tween the soil skeleton and the pore fluids, considering the anisotropic soil  
<sup>240</sup> characteristics. The soil domain is governed by a quasi-static momentum  
<sup>241</sup> balance equation for soil mixture and a mass balance equation of the pore  
<sup>242</sup> fluid based on Darcy's law. The seabed is nearly saturated, and the soil  
<sup>243</sup> skeleton generally obeys Hooke's law with elastic properties. The governing  
<sup>244</sup> equations and the solving procedure for this soil model can be referred to Li  
<sup>245</sup> et al. (2020c).

<sup>246</sup> Fig. 2 shows the sketch and flowchart of the coupled CFD model. At each  
<sup>247</sup> time step, the tsunami wave signal prescribes the dynamic wave pressure on  
<sup>248</sup> the fluid–soil interface to calculate the pore pressures and displacements in  
<sup>249</sup> the soil domain. The pore-pressure gradients are then obtained at the surfi-  
<sup>250</sup> cial seabed and transferred to the hydrodynamic and morphological modules.  
<sup>251</sup> The seepage velocities are specified at the seabed surface, which influences  
<sup>252</sup> the boundary layer and the resulting bed shear stress. Moreover, the seepage  
<sup>253</sup> forces alter the critical Shields parameter and the bed load transportation.  
<sup>254</sup> The flow drives the transport of bed and suspended loads, leading to the  
<sup>255</sup> evolving bed elevation. The underneath bed, in turn, updates the bottom  
<sup>256</sup> boundary topography by moving the computational mesh, influencing the  
<sup>257</sup> fluid dynamics. The fully coupled model is solved using the open-source  
<sup>258</sup> CFD toolbox OpenFOAM, version foam-extend 3.1. Employing a finite vol-  
<sup>259</sup> ume spatial discretization with a collocated variable arrangement, it is cou-  
<sup>260</sup> pled with a standard PIMPLE algorithm (Patankar and Spalding, 1972; Issa,  
<sup>261</sup> 1986).

#### <sup>262</sup> 2.4. Model validations

##### <sup>263</sup> 2.4.1. Velocity profile subjected to the bottom seepage

<sup>264</sup> First, we validate the present model against the experiment conducted by  
<sup>265</sup> Dey and Nath (2010) for the velocity profiles of a turbulent open-channel flow  
<sup>266</sup> over an immobile rough bed subjected to boundary injection and suction.  
<sup>267</sup> The experiment was conducted in a glass-walled rectangular flume. The  
<sup>268</sup> rough bed placed in the flume is simulated by a uniform gravel layer with a  
<sup>269</sup> median diameter  $d = 4.1$  mm and a specific gravity  $s = 2.65$ . The gravel bed  
<sup>270</sup> has a roughness length  $k_s$  of  $d$  based on velocity measurements, as reported  
<sup>271</sup> by Dey and Nath (2010). Under bed injection and suction conditions, the  
<sup>272</sup> seepage kit beneath the gravel layer produces uniformly distributed seepage  
<sup>273</sup> with velocities  $v_s = 4$  mm/s and  $v_s = -3$  mm/s, respectively. The water  
<sup>274</sup> depth  $h$  and the friction velocity  $U_f$  for the streamwise flow without the

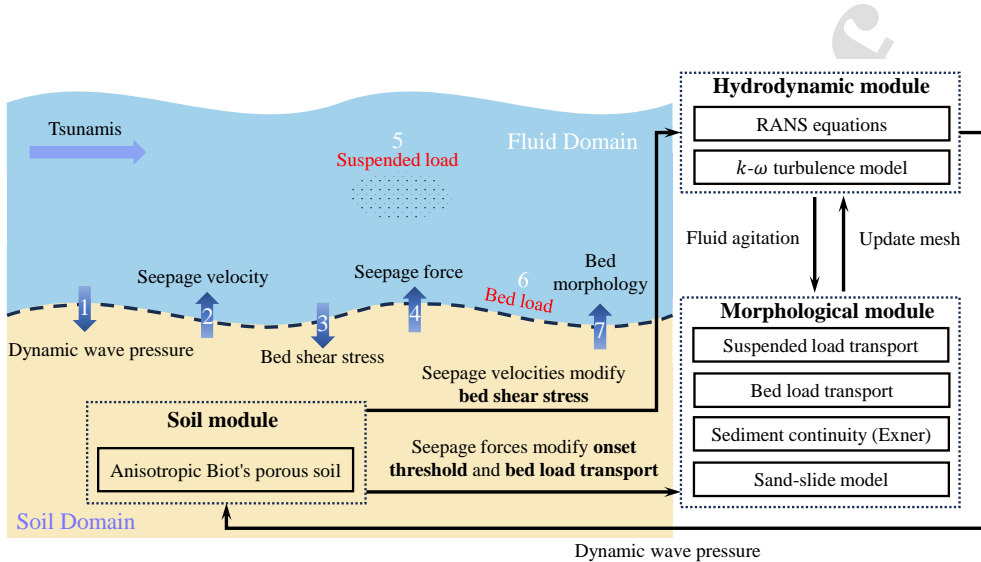


**Fig. 2.** Sketch and flowchart of the coupled CFD model. The blue arrows represent the data transfer direction, while the numbers denote the solving sequence at each time step. The free surface is shown for illustration only and is not included in the model.

275 seepage are 0.15 m and 0.033 m/s, respectively. In the present computational  
 276 flume for numerical reproduction, the smallest cells near the bed have a  
 277 height equal to  $0.5d$ . The flow is driven by the body force  $F = U_f^2/h$  and  
 278 eventually reaches a fully developed state with a separate 1DV boundary  
 279 layer simulation. Thereafter, the profiles of  $u$ ,  $k$ , and  $\omega$  are specified at  
 280 the inlet boundary of the two-dimensional simulation based on a Dirichlet  
 281 boundary condition. The seepage velocity is then applied at the bottom  
 282 boundary of the numerical flume. Fig. 3 compares the velocity profiles of the  
 283 streamwise flow,  $u_x$ , subjected to the seepage between the numerical results  
 284 and the experimental data measured at the center line of the flume. It is seen  
 285 that a good agreement is achieved for both injection and suction conditions,  
 286 especially for the water layer near the bed. The discrepancies near the water  
 287 surface might be due to the free surface effects as the Froude number based  
 288 on the water depth  $Fr \sim O(0.5)$ , see Roulund et al. (2005).

#### 289 2.4.2. Tsunami-induced scour around a monopile

290 Section 2.4.1 has validated the capability of the present model to simulate  
 291 the velocity profile of the turbulent boundary layer subjected to the bottom  
 292 seepage. To further validate the capability of tsunami scour modeling, the

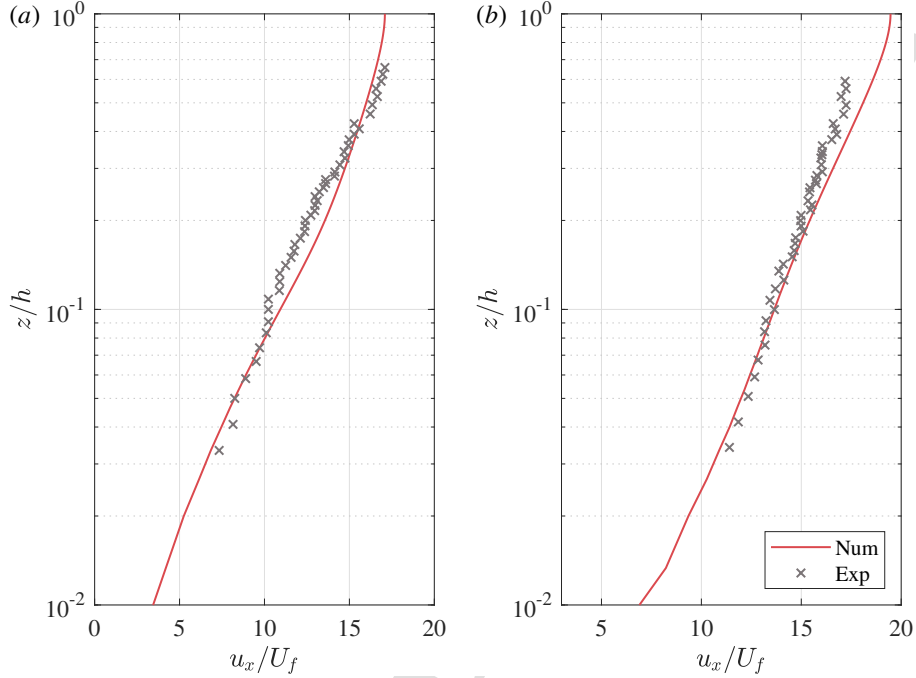


**Fig. 3.** Comparison of velocity profiles of the streamwise flow subjected to the seabed (a) suction and (b) injection between the numerical and experimental results.

laboratory experiment of Larsen et al. (2018) on the tsunami-induced scour around a monopile is numerically reproduced herein. Note that this experiment did not include seepage effects, since a pump is used to generate the flow without considering the varying wave surface. Therefore, in our simulation of this experiment, the seepage effect is excluded as well. In the physical experiment, the down-scaled tsunami is represented as a single (elongated soliton) wave with the free-stream velocity of  $U_x = U_m \operatorname{sech}^2\left(\frac{2\pi}{T}t\right)$  in a water depth  $h = 2.7D$ , where the circular pile diameter  $D = 0.1$  m. The median diameter of the sandy bed  $d = 0.18$  mm and the grain Reynolds number  $U_f d / \nu \approx 3$  as reported by Larsen et al. (2018), where  $U_f$  is the friction velocity and  $\nu$  is the kinematic viscosity. The critical Shields parameter  $\theta_{co} = 0.06$  is then used according to the classic Shields diagram with the curve fitting equation proposed by Sui et al. (2021). The present numerical simulation applies the same velocity signal as that in the experiment of Larsen et al. (2018), i.e., a single wave. Note that Larsen et al. (2018) also numerically

308 reproduced the experiment in their work, with different input parameters  
 309 compared to the present study. The critical Shields parameter they adopted,  
 310 0.05, is slightly smaller than the reality, as mentioned by Larsen et al. (2018).  
 311 Therefore, we will only compare with their experimental results here, as a  
 312 direct comparison to their numerical results is not feasible.

313 Fig. 4(a) shows the velocity profiles for the streamwise flow at the peak  
 314 with the maximum free-stream velocity  $U_m = 0.51$  m/s and the characteris-  
 315 tic wave period  $T = 123$  s. The present numerical model effectively repro-  
 316 duces the dynamics of the transient boundary layer. Notably, the boundary  
 317 layer induced by the tsunami does not extend across the entire water depth  
 318 (Williams and Fuhrman, 2016; Larsen and Fuhrman, 2019b). The experi-  
 319 mental case with  $U_m = 0.42$  m/s and  $T = 147$  s was selected for tsunami  
 320 scour validations. Fig. 4(b) compares the free-stream velocity between the  
 321 experimental and numerical results. The flow velocity in the numerical flume  
 322 is generally consistent with the experimental measurement of Larsen et al.  
 323 (2018). Some discrepancies are observed around the initial acceleration and  
 324 final deceleration phases due to the difficulties in controlling the pump to fit  
 325 the  $\text{sech}^2$  profile in the experiment (Larsen et al., 2018). Fig. 4(c) presents  
 326 the development of scour depth at the front ( $\phi = 0^\circ$ ) and front side ( $\phi = 30^\circ$ )  
 327 of the circular pile, where  $\phi$  is the angle from the center line. After several  
 328 waves in succession, the predicted scour depth gradually develops in a cu-  
 329 mulative way, which reasonably agrees with the experimental measurement,  
 330 especially for  $\phi = 0^\circ$ . Note that the scour depth at the front side of the pile is  
 331 remarkably overestimated, particularly during the first tsunami period. This  
 332 is because the bed in the experiment is not completely flat as in the compu-  
 333 tational domain, although it is leveled case by case, as reported by Larsen  
 334 et al. (2018). The small bed forms can increase the flow resistance and thus  
 335 decrease the bed shear stress compared with the model prediction (Larsen  
 336 et al., 2018). This influence fades away after several tsunami waves as the  
 337 scour depth is expected to approach equilibrium.

338 Overall, the above validations against the laboratory experiments demon-  
 339 strate the numerical model's capability to reliably predict the tsunami-induced  
 340 scour around a circular pile considering seepage effects.

### 341 2.5. Model setup and boundary conditions

342 Unless otherwise stated, the fluid computational domain has a length of  
 343  $20D$ , a width of  $15D$ , and a height of  $2.7D$ , as sketched in Fig. 5, where  $D$  is  
 344 the diameter of the circular pile. The pile fixed in the center of the domain is

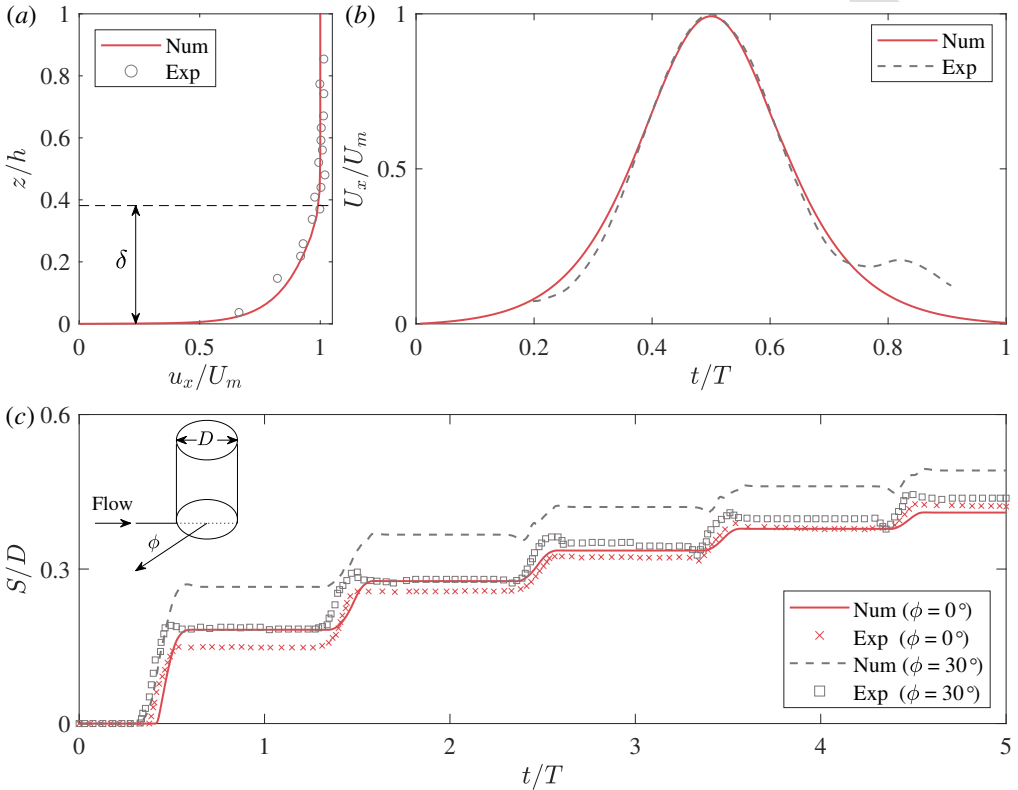


**Fig. 4.** Comparison of (a) velocity profile at the peak, (b) free-stream velocity, and (c) scour depth at the front ( $\phi = 0^\circ$ ) and front side ( $\phi = 30^\circ$ ) of a circular pile between the numerical and experimental results.

set as the origin ( $x = 0$  and  $y = 0$ ). The computational domain is spatially discretized into finite volumes with varying sizes, where the heights of the cells closest to the pile and seabed are  $0.02D$  and  $d$ , respectively, same as Larsen et al. (2017). Accordingly, the total number of cells comprising the computational mesh is 340992. During the scour calculations, the computational mesh is continuously deformed according to the evolution of seabed topography. To avoid excessive erosion caused by the flow at the boundary, the seabed is constrained near the inlet and outlet boundaries and gradually relaxed to its full morphology, i.e., the seabed topography near the inlet and outlet boundaries is fixed without mesh deformation (Baykal et al., 2015, 2017; Larsen et al., 2017, 2018). The soil computational domain has the same length and width as the fluid domain and a thickness of  $5.6D$ , where

the heights of the cells closest to the pile and seabed are  $0.02D$ .

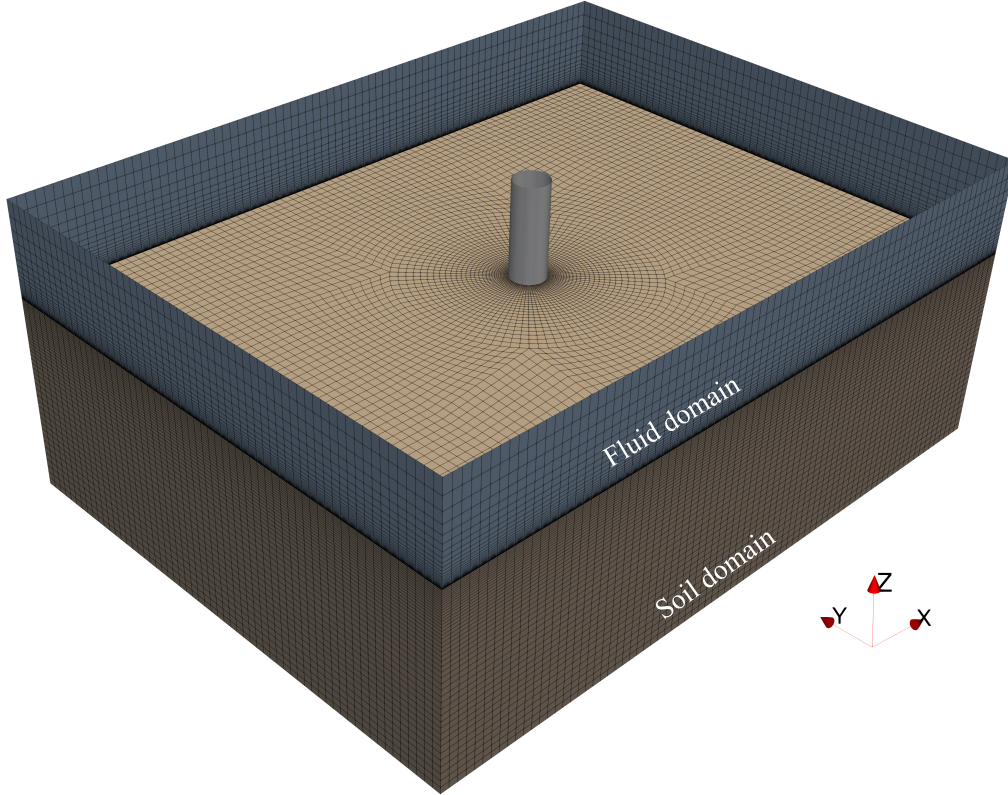


**Fig. 5.** Computational domains.

Boundary conditions for all upcoming simulations are as follows. In the fluid domain, the top of the computational domain (Fig. 5) is modeled as a frictionless slip wall, where the normal velocity component is set to zero, and the tangential component of velocity and scalar hydrodynamic quantities have a zero normal gradient. It means that we perform single-phase fluid simulations, i.e., the free surface of tsunami waves is not involved in this study. It is reasonable, provided that the Froude number based on the water depth ( $h$ ),  $Fr$ , is sufficiently low (Roulund et al., 2005).  $Fr = U_m/\sqrt{gh} = O(0.18)$  for the simulated tsunami waves shows negligible free surface effects, where  $U_m$  is the velocity magnitude and  $g$  is the gravitational acceleration. For the side boundaries, a slip boundary condition is applied for the velocity  $u$ , and a zero-gradient boundary condition is imposed for other quantities.

370 It is noted that the more complex topography (e.g., run-up on a beach) and  
 371 presence of structures are expected to affect the sinusoidal velocity signal  
 372 (Hu et al., 2023; Hu and Li, 2023). However, modeling the free surface of  
 373 the three-dimensional (3D) full-scale tsunami-scour problem gives expensive  
 374 computational costs with the advanced CFD models herein, thus we focus  
 375 only on the sediment transport process within the boundary layer. In our  
 376 3D simulations, tsunami waves are generated based on a Dirichlet condition  
 377 at the inlet boundary for the simulations with the pile. The profiles of  $u$ ,  
 378  $k$ , and  $\omega$  are derived from a separate simulation that models a 1DV pure  
 379 boundary layer in the same domain but without the pile, the same as that  
 380 in Li et al. (2020b). Neumann boundary conditions are enforced for the  
 381 other variables, while zero-gradient boundary conditions are set at the outlet  
 382 boundary, except for the pressure  $p$ , which is specified as zero.

383 The pile and seabed boundaries are modeled as no-slip hydraulically  
 384 smooth and rough walls, employing a generalized wall function approach.  
 385 The friction velocity  $U_f$  is computed from the tangential velocity at the near-  
 386 est cell center, following the profile formulated by Cebeci and Chang (1978),  
 387 which extends the work of Van Driest (1956) to account for roughness effects.  
 388 At the seabed, Nikuradse's equivalent sand grain roughness is set as  $k_s = 2.5d$   
 389 to represent hydraulic roughness, where  $d$  denotes the median diameter of  
 390 the particle. For the pile surface, a minimal value of  $k_s = 1 \times 10^{-5}$  m is  
 391 applied to signify hydraulically smooth conditions. The friction velocity is  
 392 subsequently employed for  $k$  and  $\omega$  computations in cells adjacent to the  
 393 wall. Additional details can be found in Fuhrman et al. (2014). According  
 394 to Darcy's law, the seepage velocity  $v_s = Ki$  is prescribed at the bottom  
 395 seabed boundary, including the kinematic effect of seepage flows, where  $K$  is  
 396 the soil permeability.

397 At the wave-seabed interface within the soil domain, a zero-traction con-  
 398 dition is applied to the soil, while the pore pressure is set to the dynamic wave  
 399 pressure using a Dirichlet boundary condition. At the pile-soil interface, a  
 400 zero-gradient boundary condition is imposed on the pore pressure, and soil  
 401 displacement is constrained to zero, assuming the pile is immovable. Along  
 402 the lateral boundaries of the soil, the pore pressure is assigned a zero normal  
 403 gradient, and the soil skeleton is allowed to slip. At the bottom boundary of  
 404 the soil, a zero-gradient condition is maintained for pore pressure, and the  
 405 soil skeleton is fixed with zero displacement.

**406 3. Tsunami signal and seepage response**

407 We use the advanced CFD models to investigate the full-scale tsunami  
 408 scour with three-dimensional seepage effects. The parameters of the tsunami  
 409 wave, seabed, and pile are listed in Table 1. The renowned signal of the  
 410 2004 Indian Ocean tsunami event, as recorded aboard the yacht Mercator  
 411 at a water depth of  $h = 14$  m, serves as the field tsunami scale in this  
 412 study. Madsen et al. (2008) approximated the leading wave of this signal as  
 413 a sinusoidal wave characterized by an amplitude  $A_w = 2.5$  m and a period  
 414  $T = 780$  s. The two half-cycles can be considered as an elevation wave  
 415 and depression wave (Larsen et al., 2017), respectively. Thus, the velocity  
 416 can be obtained by linear shallow water theory, i.e.,  $U_m = A_w \sqrt{g/h}$ . The  
 417 wave pressure distribution is generally assumed to vary hydrostatically under  
 418 long waves in shallow water. The dynamic wave pressure on the seabed  
 419 varies linearly with the free surface elevation  $p = \rho g A_w \sin(\frac{2\pi}{T}t)$ . A sinusoidal  
 420 model provides a more accurate representation of this tsunami event than a  
 421 solitary wave model which only accounts for positive surface displacements  
 422 and does not allow for the independent determination of effective period  
 423 and amplitude, as discussed by Madsen et al. (2008). Moreover, based on  
 424 free surface wave records from multiple locations during the 2011 Tohoku  
 425 tsunami in Japan, Chan and Liu (2012) similarly concluded that the leading  
 426 tsunami waves, both in the near-field and far-field regions, can be described  
 427 as small-amplitude long waves, aligning with the used linear shallow-water  
 428 theory (Larsen et al., 2017). The boundary layer thickness  $\delta$  is estimated by  
 429 the expression given by Williams and Fuhrman (2016) for the hydraulically  
 430 rough condition:

$$\frac{\delta}{a} = 0.05 \left( \frac{a}{k_s} \right)^{-0.11}, \quad (18)$$

431 where  $a = U_m T / 2\pi$  is the characteristic length scale. The Keulegan-Carpenter  
 432 number (Keulegan and Carpenter, 1958) is given by

$$KC = \frac{U_m T}{D}, \quad (19)$$

433 which govern the formation and excursion of the wake pattern during os-  
 434 cillatory motion. As tsunami waves propagate, the pore pressure  $p_e$  in  
 435 the underlying soil bed is estimated by the anisotropic soil model driven  
 436 by the dynamic wave pressure. The hydraulic gradient of seepage flows

<sup>437</sup>  $i = (\partial p_e / \partial x, \partial p_e / \partial y, \partial p_e / \partial z) / \rho g$  at the surficial seabed is then obtained and  
<sup>438</sup> imposed on the seabed at each time step. In our simulations, each full-  
<sup>439</sup> scale tsunami period requires approximately 20 days of computation using  
<sup>440</sup> 36 processors on the supercomputer of the National Supercomputing Centre  
<sup>441</sup> (NSCC), Singapore.

**Table 1**

Parameters of the tsunami wave, seabed, and pile.

Parameters	Value	Unit
Tsunami parameters		
Wave amplitude ( $A_m$ )	2.5	[m]
Wave period ( $T$ )	780	[s]
Water depth ( $h$ )	14	[m]
Boundary layer thickness ( $\delta$ )	3.25	[m]
Froude number ( $Fr$ )	0.18	[ $-$ ]
Keulegan-Carpenter number ( $KC$ )	653	[ $-$ ]
Reynolds number ( $Re$ )	$5.2 \times 10^6$	[ $-$ ]
Seabed parameters		
Sediment median diameter ( $d$ )	0.35	[mm]
Seabed thickness ( $h_s$ )	14	[m]
Permeability ( $K$ )	$1 \times 10^{-3}$	[m/s]
Shear modulus ( $G_s$ )	$2.64 \times 10^7$	[N/m <sup>2</sup> ]
Specific gravity ( $s$ )	2.65	[ $-$ ]
Poisson's ratio ( $\nu$ )	0.3	[ $-$ ]
Saturation factor ( $S_r$ )	0.9	[ $-$ ]
Porosity ( $n$ )	0.4	[ $-$ ]
Pile parameters		
Diameter ( $D$ )	2.5	[m]

<sup>442</sup> Fig. 6 presents the calculated pore-pressure profiles and the hydraulic  
<sup>443</sup> gradients for the full-scale tsunami. The downward pressure force can be  
<sup>444</sup> observed during the elevation wave, while the upward pressure force is exerted  
<sup>445</sup> on the upper soil during the depression wave. Fig. 7(a) presents the free-  
<sup>446</sup> stream velocity during the tsunami propagation on a fixed flatbed. The  
<sup>447</sup> corresponding surficial seepage response at the front of the circular pile is  
<sup>448</sup> sequentially suction (flow into the bed) and injection (flow out of the bed).

449 The  $x$ - and  $y$ -directed hydraulic gradients are negligible compared with the  
 450 vertical direction. Fig. 7(b) shows the tsunami-induced Shields parameter  
 451  $\theta_o$  (Eq. 17) and critical Shields parameter  $\theta_{co}$  (Eq. 5) at the flatbed. The  
 452 “seepage-on” case considers the seepage response induced by the tsunami  
 453 loading in the underlying soil. The “seepage-off” case is a control group  
 454 without considering the seepage. Compared with the “seepage-off” case,  
 455 the seabed suction increases both the bed shear stress ( $\theta_o$ ) and critical bed  
 456 shear stress ( $\theta_{co}$ ). However, the seabed injection shows the opposite effect.  
 457 The competing trends of the fluid–sediment momentum transfer and onset  
 458 threshold of sediment motion influence the tsunami-induced sediment (Hu  
 et al., 2024).

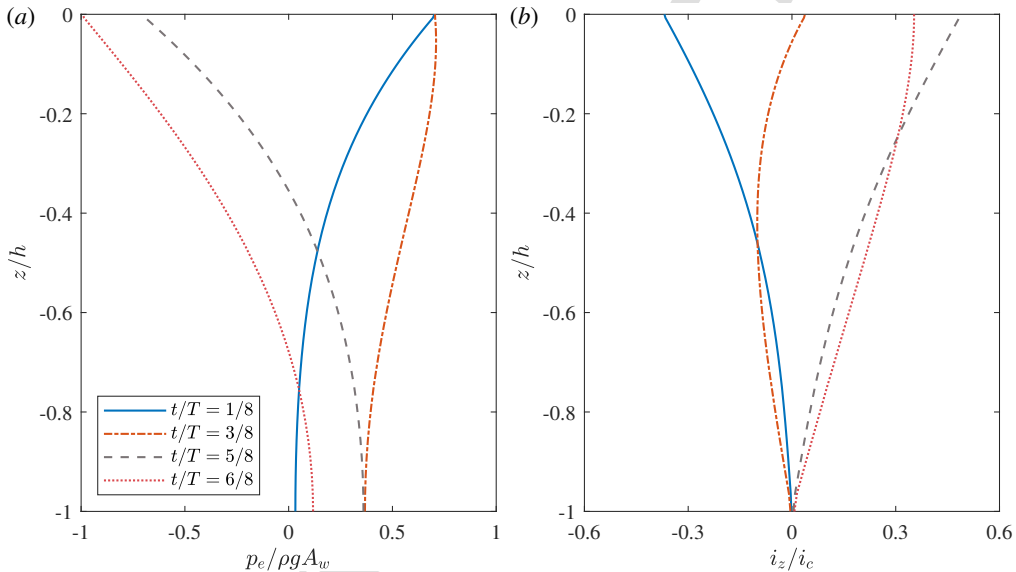


**Fig. 6.** Tsunami-induced (a) pore-pressure head profiles and (b) vertical hydraulic gradient  $i_z$  profiles at the front of the pile.

459

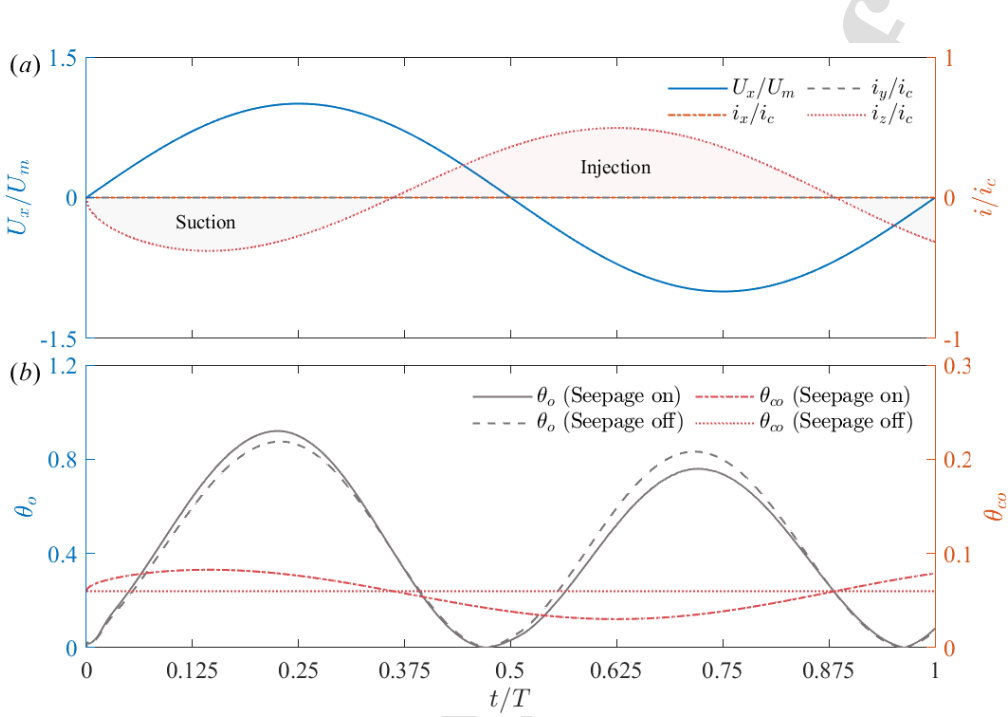


**Fig. 7.** Tsunami-induced (a) free-stream velocity and corresponding surficial hydraulic gradient at the front of the pile, (b) Shields parameter, and critical Shields parameter at the flatbed.

#### 4. Seepage effects on tsunami flow features around a circular pile

In this section, we conduct full-scale rigid-bed simulations to investigate the effects of dynamic seepage response on main flow characteristics around a vertical slender pile subjected to tsunamis, i.e., separate horseshoe vortices formed in front and back of the pile during successive half cycles, lee-side vortices in the form of vortex shedding, and contracted streamlines around the side edges of the pile (Sumer and Fredsøe, 2002, pp. 150-151).

##### 4.1. Horseshoe vortex

The horseshoe vortex around a circular pile exposed to flow can tremendously amplify the bed shear stress relative to its undisturbed value (Baker, 1979; Hjorth, 1975; Roulund et al., 2005; Baykal et al., 2017), which mainly influences the scouring processes. The horseshoe vortex is induced by the combined action of approach flow rotation and adverse pressure gradient

473 caused by the presence of the pile (Sumer and Fredsøe, 2002). The bound-  
 474 ary layer separates and forms a spiral vortex around the pile, trailing off  
 475 downstream. The size of the horseshoe vortex in front of a circular pile in  
 476 the context of waves is mainly determined by three factors: the ratio of bed  
 477 boundary layer thickness to the pile diameter  $\delta/D$ ; the ratio of bed rough-  
 478 ness to the pile diameter  $k_s/D$ ; and Keulegan-Carpenter number  $KC$  (Baker,  
 479 1979; Sumer and Fredsøe, 2002). Due to the large  $KC$  number of the simu-  
 480 lated tsunami waves in the present study (see Table 1), the wave excursion is  
 481 large enough that the flow during each half cycle resembles a steady current.  
 482 Consequently, the horseshoe vortex beneath tsunamis is expected to behave  
 483 similarly to that in a current (Larsen et al., 2017, 2018).

484 Fig. 8 displays the instantaneous vortical structures represented by the  $Q$   
 485 iso-surfaces around the pile with and without considering the seepage effects,  
 486 identified by the so-called  $Q$ -criterion (Hunt et al., 1988). The  $Q$ -criterion  
 487 identifies a vortex as a coherent fluid region exhibiting a positive second  
 488 invariant ( $Q > 0$ ) of the velocity gradient tensor:

$$489 \quad Q = \frac{1}{2} (|\Omega_{ij}|^2 - |S_{ij}|^2) > 0 \quad (20)$$

490 that is the region where the magnitude of the mean rotation tensor  $\Omega_{ij}$  pre-  
 491 vails over the magnitude of the strain-rate tensor  $S_{ij}$ , where

$$492 \quad \Omega_{ij} = \frac{1}{2} \left( \frac{\partial u_i}{\partial x_j} - \frac{\partial u_j}{\partial x_i} \right), S_{ij} = \frac{1}{2} \left( \frac{\partial u_i}{\partial x_j} + \frac{\partial u_j}{\partial x_i} \right). \quad (21)$$

493 As shown in Fig. 8(a,b), the free-stream flow is from left to right and reaches  
 494 the peak velocity at  $t/T = 0.25$ . The horseshoe vortex in front of the cir-  
 495 cular pile and lee-wake shed vortices at the back are observed in the flow  
 496 visualization. In the presence of the seabed suction, the size of the horse-  
 497 shoe vortex barely decreases compared to that of the impermeable bed. In  
 498 Fig. 8(c,d), the free-stream flow reverses and peaks at  $t/T = 0.75$ . The  
 499 size of the horseshoe vortex with the seabed injection marginally increases  
 500 compared to that without considering the seepage effects. These trends will  
 501 be more clearly shown in the characteristic length  $x_s$  of the horseshoe vor-  
 502 tex depicted in Fig. 10 and the upward-directed pressure gradient inside the  
 503 horseshoe vortex illustrated in Fig. 11. The decrease/increase in the size of  
 504 the horseshoe vortex is because of the decrease/increase of boundary layer  
 505 thickness caused by the seabed suction/injection, as shown in Fig. 9. The

variations in the boundary layer thickness are more pronounced with the seabed injection during the depression wave. The separation of the seabed boundary layer will be delayed if the ratio of boundary layer thickness to the pile diameter  $\delta/D$  decreases (Baker, 1979; Sumer et al., 1997; Sumer and Fredsøe, 2002, pp. 153-154), presumably leading to a smaller-size horseshoe vortex. The visible lee-side vortices will be discussed in Section 4.2.

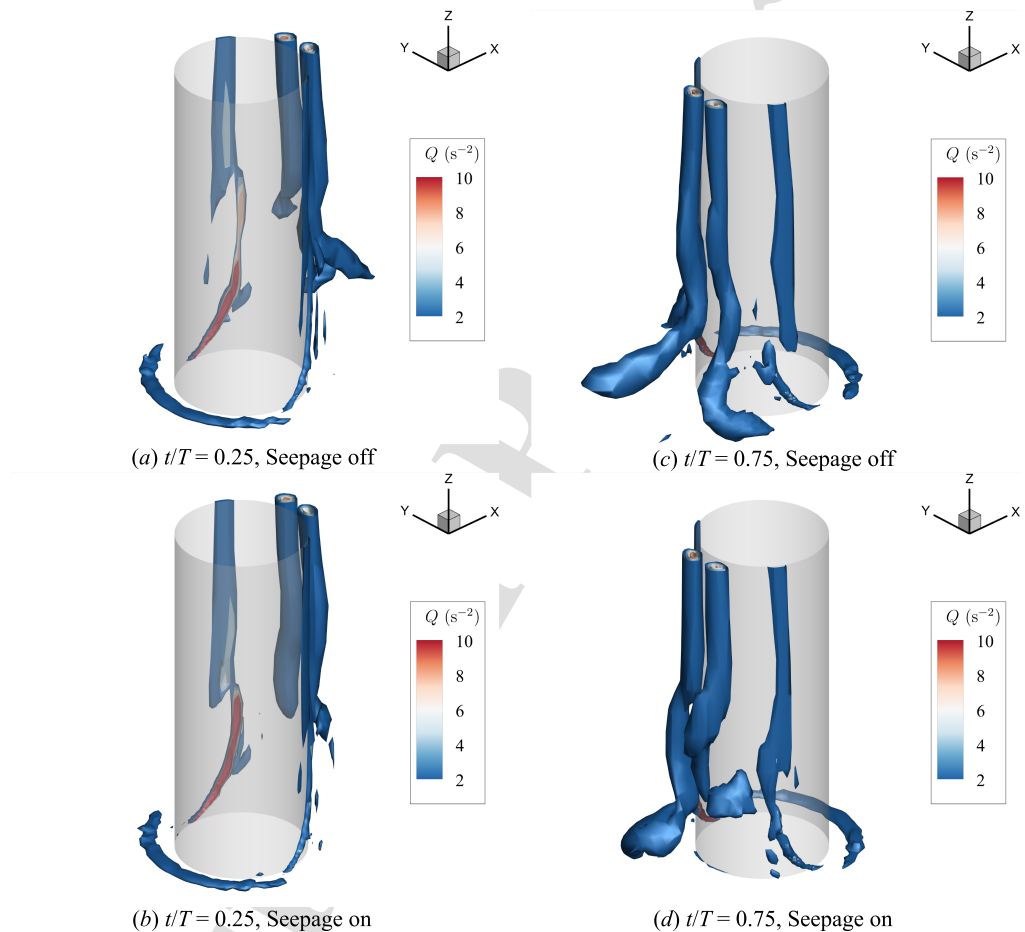


**Fig. 8.**  $Q$  representations for the horseshoe vortex and the shed vortices around the circular pile at  $t/T = 0.25$  and  $t/T = 0.75$  (a,c) without and (b,d) with considering the seepage effects.

Fig. 10(a) shows the variation of bed shear stress amplification  $\tau/\tau_o$  along the  $x$ -axis at the horseshoe vortex side of the circular pile, where  $\tau$  is the local

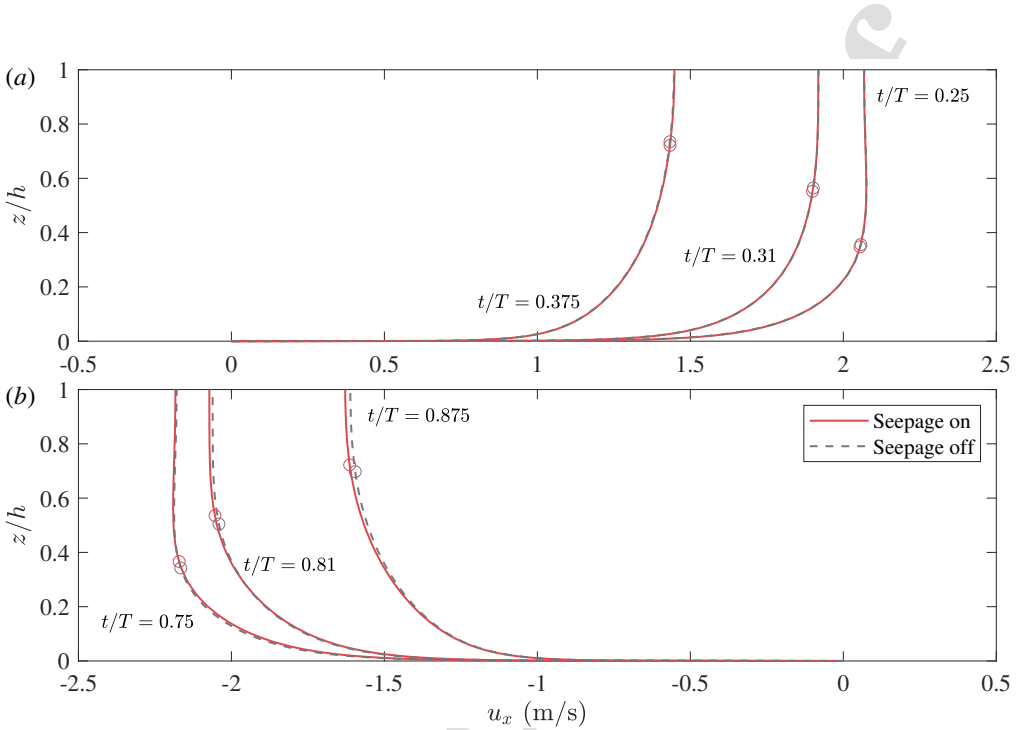


**Fig. 9.** Velocity profiles at different times during the (a) elevation and (b) depression with and without considering the seepage effects, where (o) marks the boundary layer thickness.

bed shear stress and  $\tau_o$  is the undisturbed bed shear stress in the far velocity field. The negative  $\tau/\tau_o$  represents the position of the horseshoe vortex in the streamwise direction at the incoming flow side. The distance  $x_s$  from the zero-crossing of the bed shear stress to the pile center is defined as the length that characterizes the size of the horseshoe vortex. At  $t/T = 0.25$  ( $x/D < 0$  in front of the pile), the seabed suction barely decreases  $x_s$  and  $\tau/\tau_o$ , as compared to the impermeable seabed. At  $t/T = 0.75$  ( $x/D > 0$  at the back of the pile), the seabed injection marginally increases the size of the horseshoe vortex and the amplification of bed shear stress within it. Note that the bed shear stress inside the horseshoe vortex might be underpredicted as the coherent structures can be damped or smoothed by the RANS simulations (Baykal et al., 2017).

Fig. 11 illustrates the vertical pressure gradient  $-\partial(p/\rho)/\partial z$  fields in  $y-z$  planes at  $x = x_r$  (left panels) and  $x = x_d$  (right panels) given in Fig. 10(a). The upper downward-directed pressure gradient (negative  $-\partial(p/\rho)/\partial z$  val-

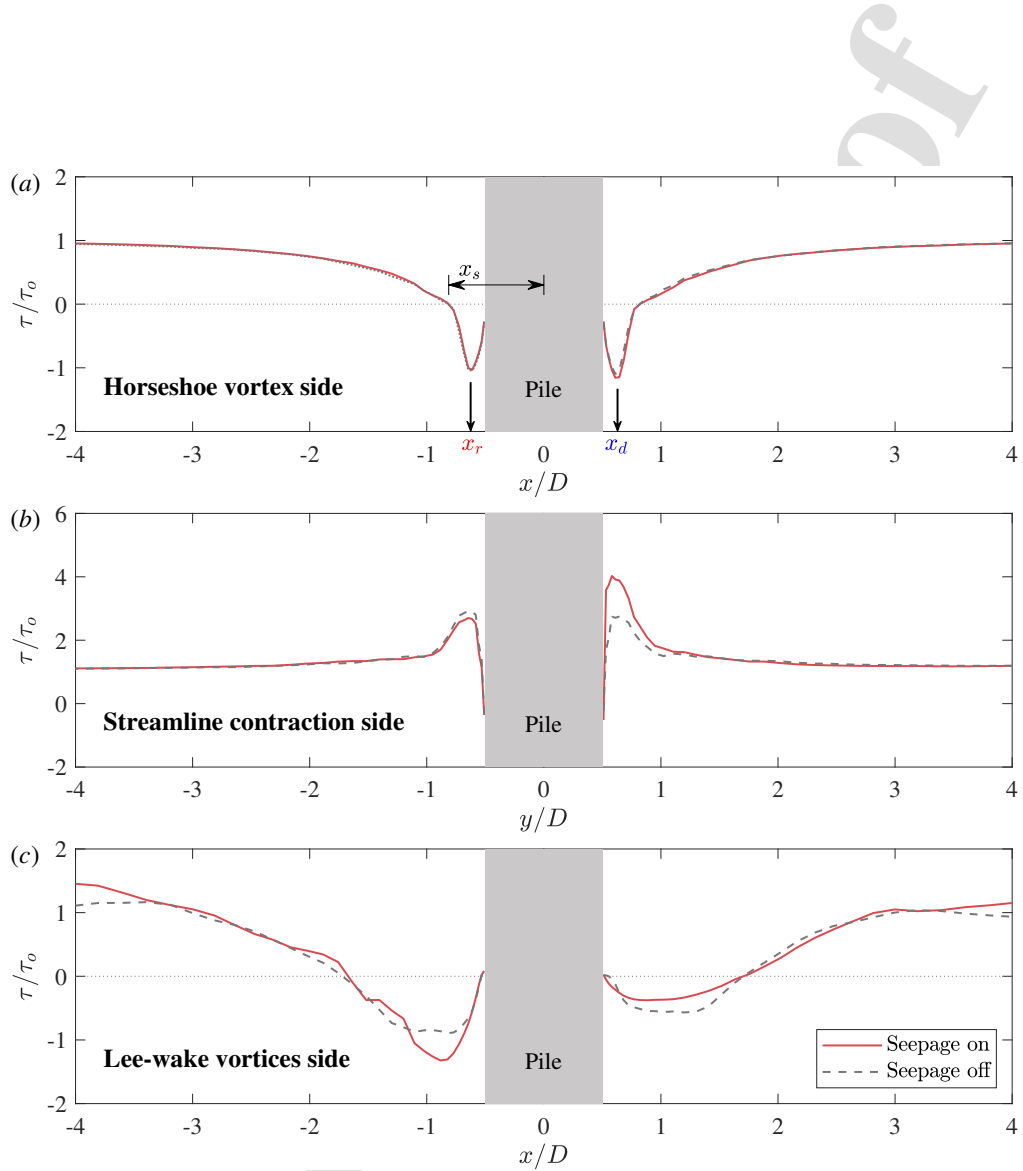


**Fig. 10.** Amplification of bed shear stress along the  $x$ -axis at the (a) horseshoe vortex side (at  $t/T = 0.25$  for  $x/D < 0$  and  $t/T = 0.75$  for  $x/D > 0$ ), (b) streamline contraction side (at  $t/T = 0.25$  for  $y/D < 0$  and  $t/T = 0.75$  for  $y/D > 0$ ), and (c) lee-wake vortices side (at  $t/T = 0.75$  for  $x/D < 0$  and  $t/T = 0.25$  for  $x/D > 0$ ) of the circular pile.

ues) causes the downflow due to the deceleration of the approach flow. The upward-directed pressure gradient (positive  $-\partial(p/\rho)/\partial z$  values) on the seabed corresponds to the position of the horseshoe vortex in the vertical direction. The upward-directed pressure gradient can drive sediment suspension via upward vertical flow (Baykal et al., 2015). In Fig. 11(a,b), the upward-directed pressure gradient with the seabed suction is marginally less pronounced than that without considering the seepage effects. This, combined with the increased onset threshold of sediment transport shown in Fig. 7(b), can marginally reduce the scour at the front of the circular pile during the elevation wave. More details will be shown in Section 5.1. In Fig. 11(c,d), the seabed injection yields a marginally greater area and magnitude of the upward-directed pressure gradient than that without considering the seepage effects. The differences in the instantaneous  $-\partial(p/\rho)/\partial z$  field between  $x = x_d$  and  $x = x_r$  is due to the slight phase shift between the boundary layer and the free-stream flows, which also can be seen between  $\theta_o$  and  $U_x$  in Fig. 7(a,b). Overall, the seepage response shows insignificant effects on the size and intensity of the horseshoe vortex in front and back of the circular pile.

#### 545 4.2. Streamline contraction and lee-wake vortices

546 Fig. 10(b) depicts the amplification of bed shear stress  $\tau/\tau_o$  along the  
 547  $y$ -axis near the side edges of the circular pile. The contraction of the stream-  
 548 lines essentially determines the amplification of the positive bed shear stress.  
 549 The maximum  $\tau/\tau_o$  is reduced by 8% due to the seabed suction, while it is  
 550 increased to  $O(4)$  since  $\tau_o$  with the seabed injection decreases more obviously  
 551 as shown in Fig. 7(b). The variations of the bed shear stress caused by the  
 552 seepage response can potentially influence the sediment transport near the  
 553 side edges of the circular pile, which will be shown in Section 5.1. Note that  
 554 the span with amplified bed shear stress ( $\tau/\tau_o > 1$ ) is very similar between  
 555 the “seepage-on” and “seepage-off” cases regardless of the seepage direction.

556 We then investigate the seepage effects on the lee-wake vortices of the  
 557 circular pile in tsunami waves. The formation of lee-wake vortices is primar-  
 558 ily caused by the rotation within the boundary layer over the surface of a  
 559 pile. The shear layers that originate from the side edges of the pile roll up  
 560 and create these vortices in the lee wake of the pile (Sumer and Fredsøe,  
 561 2002; Baykal et al., 2017). The Reynolds number  $Re = U_m D/\nu$  of present  
 562 tsunami waves is  $5.2 \times 10^6$ , which implies that the vortex shedding occurs in

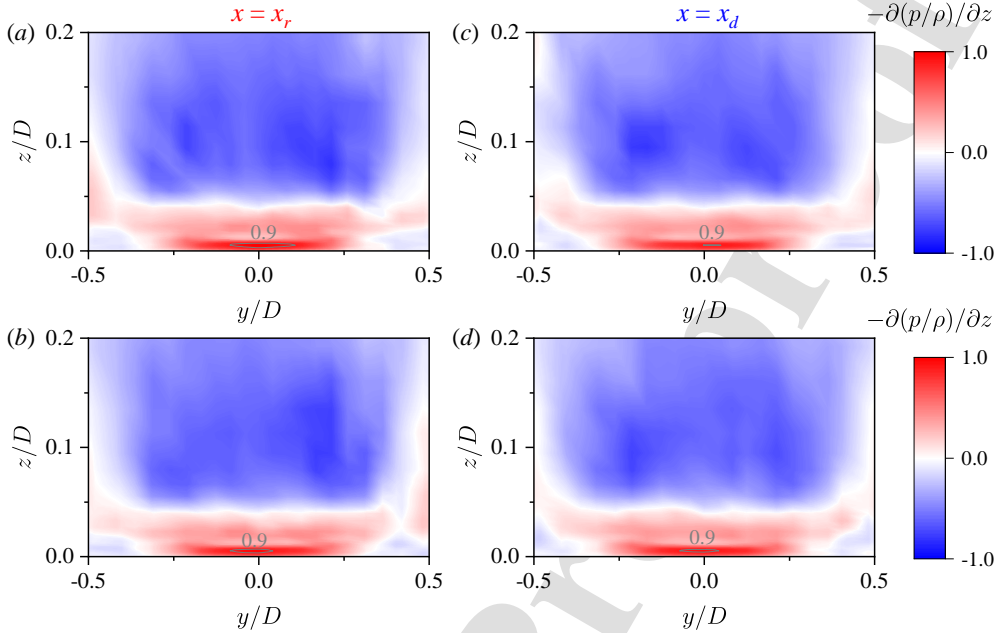


**Fig. 11.** Vertical pressure gradient fields at the longitudinal sections ( $y$ - $z$  planes) given in Fig. 10(a) for the seabed (a,c) without and (b,d) with considering the seepage effects.

the turbulent regime (Sumer, 2006). Fig. 8 illustrates that the vortex shedding occurs in a two-cell regime over the height of the pile, as the velocity profiles of the approach flow are not uniform from the seabed to the upper water column. The two-cell regime refers to the vortical structures breaking into two parts along the pile; one moves slowly close to the seabed, while the upper rest resembles the lee-wake vortices of a free cylinder (Baykal et al., 2015). The lee-wake vortices of a circular pile in tsunami waves behave both current-like due to the existence of the two-cell vortical structures (Baykal et al., 2015) and wave-like due to the insignificant counter-rotating vortices near the seabed (Baykal et al., 2017). The two-cell vortical structures are more visible in the side view of the position of boundary layer separation in Fig. 12, where the streamwise velocity reverses along the vertical pile. The lower cell extends up to  $z/D = 1.0$  from the seabed, similar to that in a steady current studied by Baykal et al. (2015). At  $t/T = 0.25$  ( $x/D > 0$  at the lee side of the pile), the effect of seabed suction on the boundary layer

separation is minimal. At  $t/T = 0.75$  ( $x/D < 0$  in front of the pile), the seabed injection slightly advances the boundary layer separation. The thickness of the tsunami boundary layer experiencing seabed injection increases, as shown in Fig. 9, reducing momentum exchange between the outer flow and the hydraulically rough seabed. Consequently, the decreased streamwise momentum in the boundary layer leads to earlier separation.

Fig. 10(c) depicts the bed shear stress amplification along the  $x$ -axis at the lee-wake vortices side of the circular pile. In the absence of seepage response, the amplification in the bed shear stress concerning its undisturbed value can be  $O(0.7)$  during the tsunami propagation. At  $t/T = 0.25$  ( $x/D > 0$ ), the bed shear stress amplification  $\tau/\tau_o$  underneath the lee-wake vortices generally decreases when considering the seabed suction. At  $t/T = 0.75$  ( $x/D < 0$ ),  $\tau/\tau_o$  shows an opposite trend in the presence of seabed injection. The abovementioned variations of boundary layer separation position over the pile cause the seepage effects to extend to a few pile diameters at the lee-wake vortices side. Overall, the seepage response to tsunami loading exhibits more obvious effects on the amplification of bed shear stress at the streamline contraction and lee-wake vortices sides than the horseshoe vortex side.

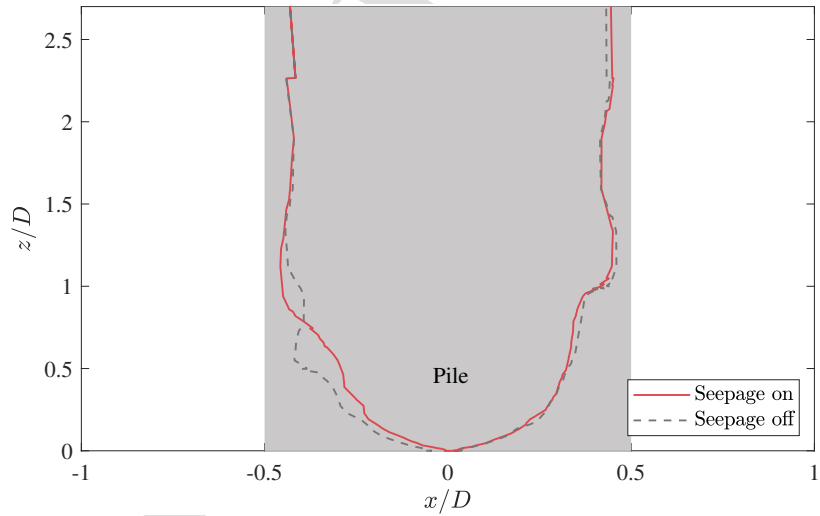


**Fig. 12.** Position of boundary layer separation (at  $t/T = 0.75$  for  $x/D < 0$  and  $t/T = 0.25$  for  $x/D > 0$ ) over the height of the pile.

595

596    *4.3. Amplification of bed shear stress*

597    The amplification of bed shear stress along the  $x$ - and  $y$ -axes has been  
 598    discussed for the horseshoe vortex side in Section 4.1 and for the streamline  
 599    contraction and lee-wake vortices sides in Section 4.2. This section illustrates  
 600    the overall picture of bed shear stress amplification around the pile with and  
 601    without considering seepage effects, as shown in Fig. 13, where the amplifi-  
 602    cation of bed shear stress herein is the ratio of the maximum magnitude of  
 603    the bed shear stress vector to the undisturbed bed shear stress  $|\tau_{max}|/\tau_{o,max}$ .

604    In Fig. 13(a), the maximum amplification in bed shear stress appears at  
 605    the front side ( $\phi \approx 60^\circ$ ) of the pile. In the absence of seepage flows, the bed  
 606    shear stress can be as much as a factor of 6 larger than the undisturbed bed  
 607    shear stress, which falls between  $O(3\text{--}4)$  in wind-generated waves and  $O(10)$   
 608    in a steady current (Sumer et al., 1997; Sumer and Fredsøe, 2002; Baykal  
 609    et al., 2015, 2017). The maximum amplification is mainly determined by the  
 610    combined effect of the horseshoe vortex and the contraction of streamlines,  
 611    which is similar to but less significant than that of a steady current in Sumer  
 612    and Fredsøe (2002). The amplification fields are almost symmetric as the  
 613    tsunami signal is sinusoidal. The seepage response leads to the asymmetric  
 614     $|\tau_{max}|/\tau_{o,max}$ , as shown in Fig. 13(b). This is mainly due to the variations of  
 615     $\tau_{o,max}$  in the far field. The maximum amplification decreases at the front side  
 616    of the pile, while it increases to  $O(8)$  at the back side ( $\phi \approx 120^\circ$ ). The increase  
 617    in amplification can naturally induce a rapid scour near this region, combined  
 618    with the decrease in the onset threshold of sediment transport caused by the  
 619    seabed injection shown in Fig. 7(b). The stronger tsunami scour at the side  
 620    of the pile with the seabed injection will be shown in Section 5.1.

621    Overall, the amplification of bed shear stress during tsunami propaga-  
 622    tion is intermediate between wind-generated waves and a steady current.  
 623    The seepage response to tsunami loading yields a notable difference in the  
 624    amplification between the elevation and depression. Specifically, the seabed  
 625    injection during the depression wave primarily governs the maximum ampli-  
 626    fication.

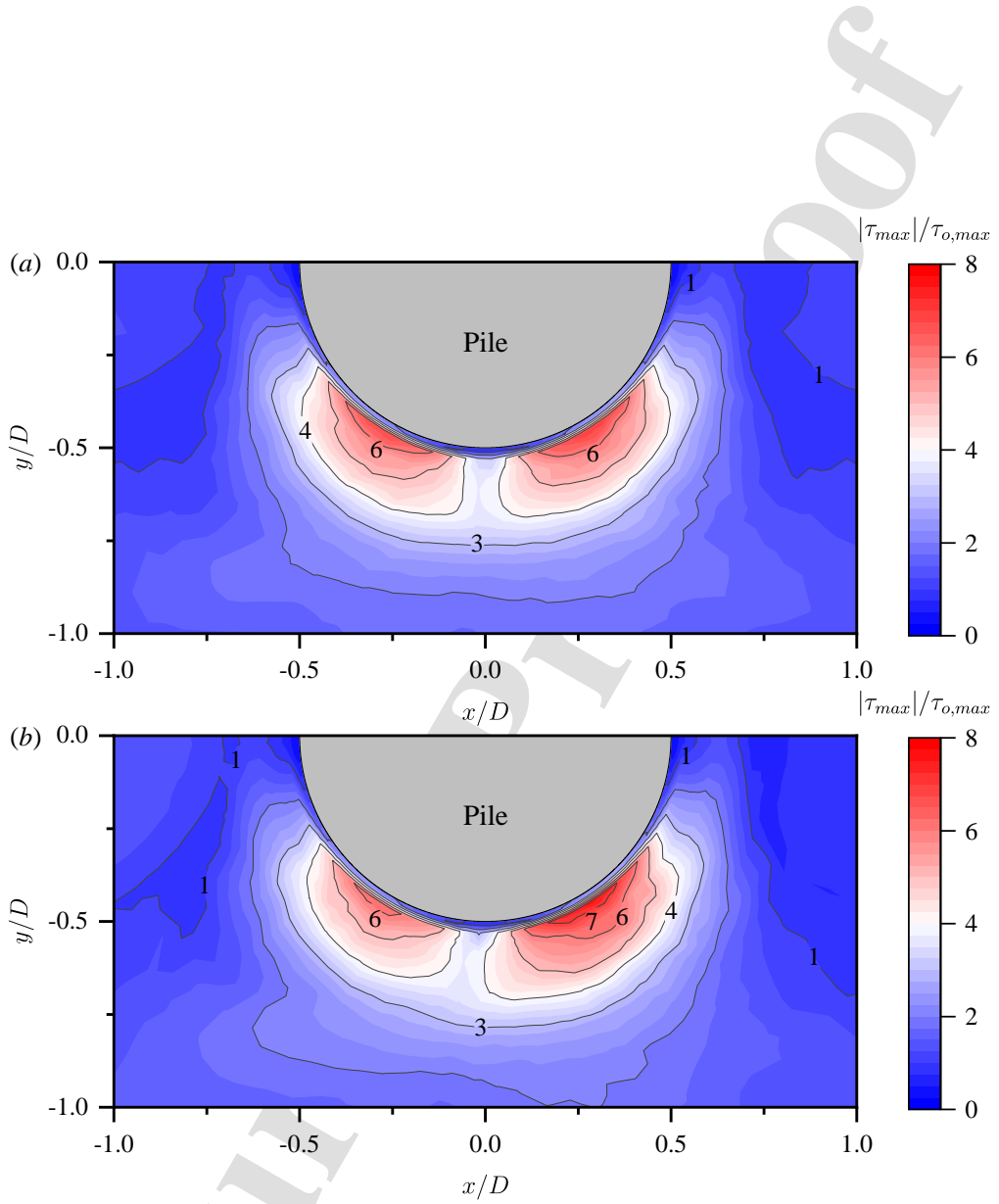


**Fig. 13.** Amplification of bed shear stress around the circular pile (a) without and (b) with considering the seepage.

## 627 5. Seepage effects on tsunami-induced scour around a circular pile

628 In this section, we investigate the effects of seepage response on tsunami-  
 629 induced scour around a circular pile by enabling the seabed morphological  
 630 evolution in the present fully coupled CFD model. In Section 5.1, the evo-  
 631 lution of the scour depth and seabed topography is compared between cases  
 632 with and without considering the seepage effects during the tsunami propa-  
 633 gation. In Section 5.2, we present the seepage effects on sediment transport  
 634 rate to elaborate the tsunami scour mechanisms.

### 635 5.1. Tsunami scour evolution

636 Fig. 14 shows the temporal variation of the scour depth  $S/D$  at different  
 637 pile positions during the tsunami propagation. In Fig. 14(a) at the front  
 638 ( $\phi = 0^\circ$ ) of the pile, the scour hole gradually deepens and then reaches  
 639 a temporary equilibrium stage around  $t/T = 0.375$ . The seabed suction  
 640 marginally reduces the temporary equilibrium scour depth. This is mainly  
 641 because of the increased onset threshold of sediment transport as shown in  
 642 Fig. 7(b). After the flow reversal, the scour depth with and without the  
 643 seepage effects tends to be indistinguishable. In Fig. 14(b) at the side ( $\phi =$   
 644  $90^\circ$ ) of the pile, the scour depth starts to grow more rapidly from the peak  
 645 seabed suction intensity, compared to the impermeable bed. The temporary  
 646 equilibrium scour depth is slightly reduced by 10%, which is primarily owing  
 647 to the combination of the lower bed shear stress amplification underneath the  
 648 contraction of streamlines as shown in Fig. 10(b) and the increased critical  
 649 Shields parameter as shown in Fig. 7(b). During the depression wave, the  
 650 scour hole experiences a rapid backfilling, followed by further erosion in the  
 651 reversed flow. It is observed that the final scour depth after one tsunami wave  
 652 cycle is lower when considering the seepage response. This is owing to the  
 653 more deposition emanating from the stronger scour at the back ( $\phi = 180^\circ$ )  
 654 of the pile, as shown in Fig. 14(c). Specifically, the rapid scour occurs at  
 655 the end of the depression wave, when the flow velocity is decreasing. This is  
 656 because of the enhanced suspended load transport, which will be discussed  
 657 in Section 5.2. The rapid scour at the back of the pile during the end of  
 658 tsunami draw-down was also reported in a large-scale experimental study on  
 659 tsunami scour around a cylinder (Tonkin et al., 2003). Consequently, the  
 660 temporary equilibrium scour depth with the seepage response increases by  
 661 16%, compared to the impermeable seabed.

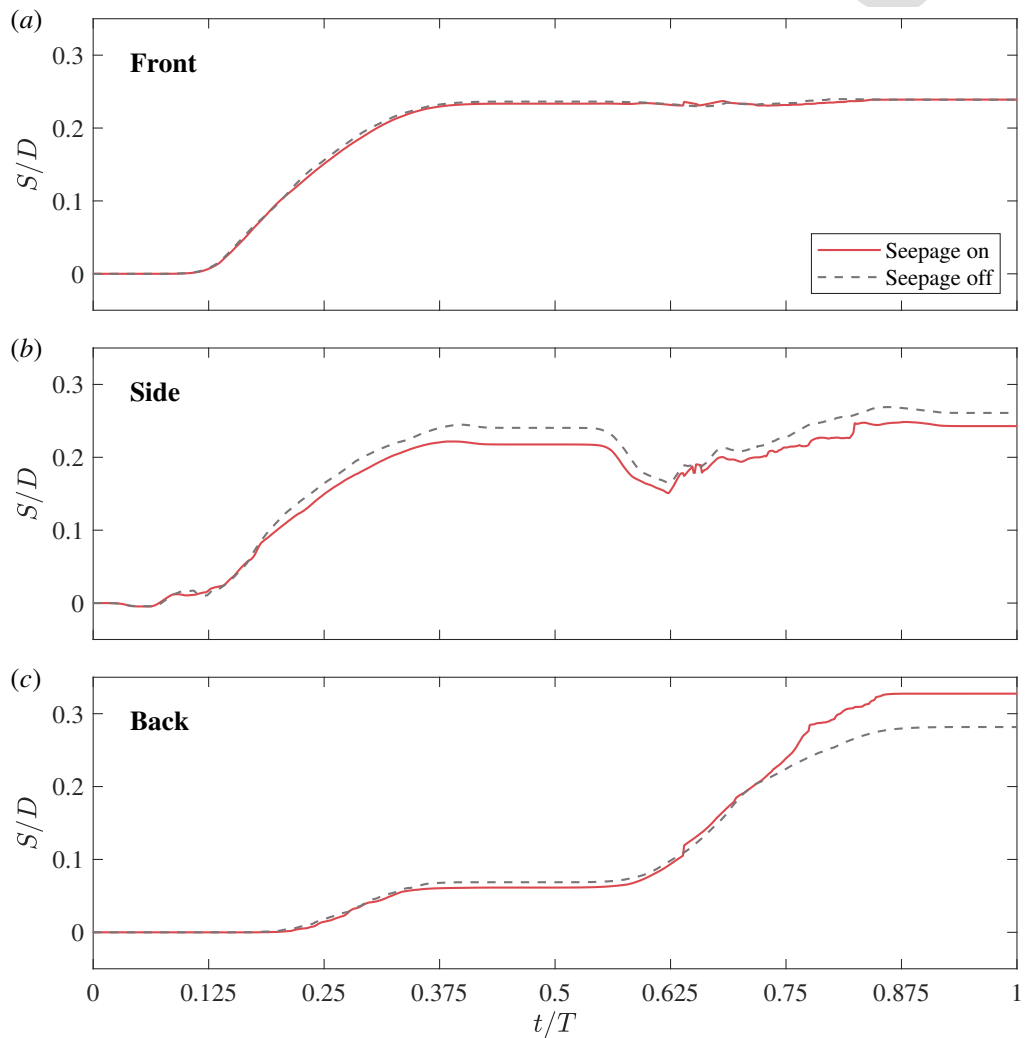
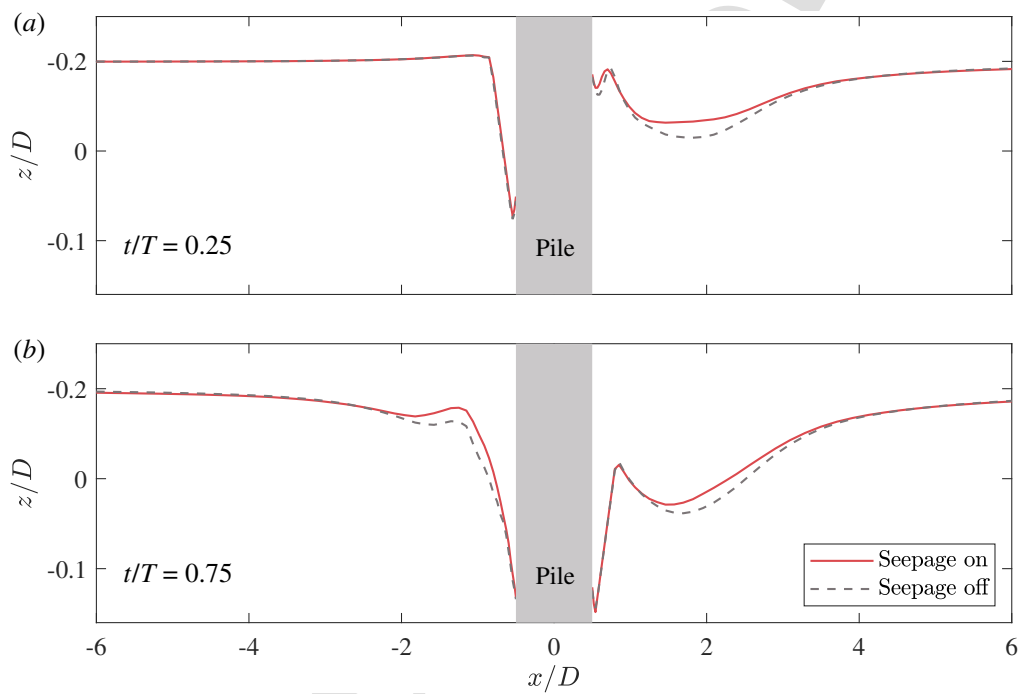


**Fig. 14.** Scour depth at the (a) front ( $\phi = 0^\circ$ ), (b) side ( $\phi = 90^\circ$ ), and (c) back ( $\phi = 180^\circ$ ) of the circular pile without and with considering the seepage.

Overall, the computed development of scour depth at the front, side, and back of the circular pile with seepage effects is very similar to the trends of experimental observations in Tonkin et al. (2003), which indicates the capability of the present CFD model in predicting the tsunami scour. Since the present numerical model does not take into account the variations of wave free surface, e.g., wave shoaling and breaking phenomena involved in their tests, a direct comparison with their experimental results is not feasible.

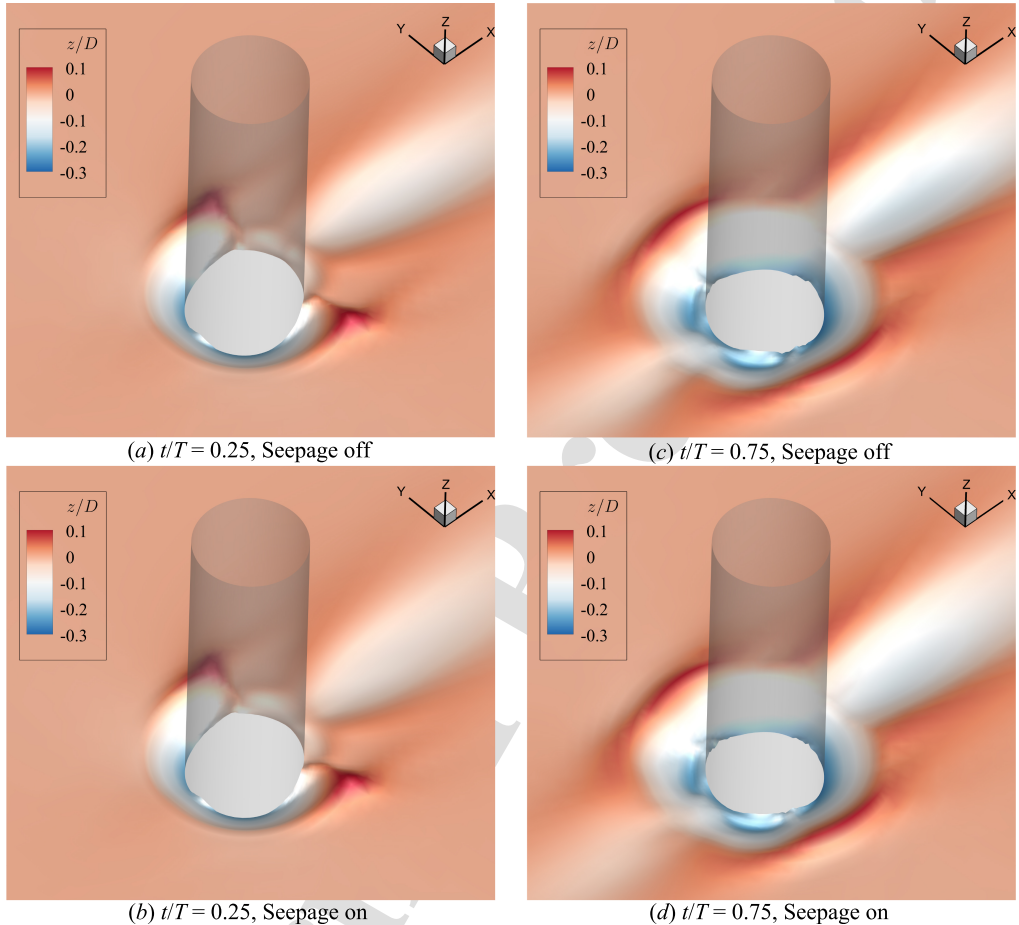
Fig. 15 presents the scour profiles along the center line of the circular pile with and without considering seepage effects. At  $t/T = 0.25$  (see Fig. 15a), the scour hole in front of the pile ( $x/D < 0$ ) has a slope angle  $\beta = 31.4^\circ$  close to the angle of repose  $\beta_r = 32^\circ$  of the sediment grains. The scour profiles almost overlap into a single line, owing to the indistinguishable horseshoe vortex with and without seepage, as discussed in Section 4.1. In contrast, the scour hole at the back of the pile ( $x/D > 0$ ) is shallower in the presence of seabed suction, which is due to the decreased bed shear stress amplification underneath the lee-wake vortices as shown in Fig. 10(c), and the increased critical Shields parameter as shown in Fig. 7(b). At  $t/T = 0.75$  (see Fig. 15b), the scour hole within the horseshoe vortex at the back of the pile ( $x/D > 0$ ) marginally increases when considering the seepage. A sandbar forms in front ( $x/D < 0$ ) of the pile, and its formation and migration are due to the large-scale counter-rotating streamwise vortices in the lee wake (Baykal et al., 2015). When considering the seepage effect, the sandbar is more pronounced because of the enhanced deposition shown in Fig. 14.

Fig. 16 depicts the seabed topography around the circular pile with (lower panels) and without (upper panels) the seepage effects. At  $t/T = 0.25$ , a semi-circular scour hole with a steep slope forms around the upstream side of the circular pile, see Fig. 16(a,b). The sediment is deposited behind both sides of the pile, creating two sandbars with steeper slopes. A strip-like scour hole is visible between these two sandbars due to vortex shedding, trailing downstream (right-hand boundary side) of the pile. These scouring features are marginally less pronounced in the presence of seabed suction. At  $t/T = 0.75$ , the scour hole around the side and back of the pile deepens further following the flow reversal. As a result, the scour hole around the pile resembles an inverted frustum shape. Additionally, the sandbars behind the pile are eroded as they are more exposed to the approach flow, migrating upstream. The sediment is deposited into two sandbars alongside the pile. Moreover, the front scour hole is gradually backfilled. The backfilling and sandbars are more noticeable for the “seepage-on” scenario due to the



**Fig. 15.** Scour profiles along the center line of the circular pile at (a)  $t/T = 0.25$  and (b)  $t/T = 0.75$  without and with considering seepage effects.

700 increased scour caused by the seabed injection. The erosion caused by the lee-wake vortices becomes visible in front of the pile.



**Fig. 16.** Bed topography around the circular pile at  $t/T = 0.25$  and  $t/T = 0.75$  (a,c) without and (b,d) with considering seepage effects.

701  
 702 The seepage response to the tsunami loading can affect the scour pro-  
 703 cesses. The sediment redistribution caused by the seepage response can im-  
 704 pact the main focus of scour protection in coastal and offshore areas, e.g., the  
 705 rapid scour near the back of the monopile during the depression tsunami wave  
 706 potentially leads to a foundation failure or bridge collapse.

707    5.2. Tsunami-induced sediment transport rate

708    In the present simulations of the seabed morphological evolution, the hy-  
 709    drodynamic flow conditions and onset threshold of sediment transport evolve  
 710    simultaneously and continuously because of the disturbance of the structure  
 711    and variations of bed slopes. To further elucidate the seepage effects on  
 712    the tsunami scour, we investigate the tsunami-induced sediment transport  
 713    rate during the scour development with and without considering the seep-  
 714    age. Fig. 17 shows the temporal variation of bed, suspended, and total load  
 715    transport rates  $q_b$ ,  $q_s$ , and  $q_t$  at the front ( $t/T < 0.5$ ) and back ( $t/T > 0.5$ ) of  
 716    the pile. During the elevation wave, the bed load transport rate at the front  
 717    side of the pile is generally lower in the presence of seabed suction, as seen  
 718    in Fig. 17(a). This is mainly due to the competing effects of seabed suction  
 719    on the bed mobility discussed in Section 3, combined with the marginally  
 720    weakened horseshoe vortex shown in Section 4.1. The suspended load trans-  
 721    port rate is also generally decreased compared to the impermeable seabed, as  
 722    illustrated in Fig. 17(b). Note that the suspended load transport dominates  
 723    sediment transport during the full-scale tsunami propagation. Consequently,  
 724    the total load transport rate is lower when considering the seepage response,  
 725    as shown in Fig. 17(c). During the depression wave, the seabed injection  
 726    intensifies the sediment transport at the back side of the pile, especially  
 727    for the suspended load, as shown in Fig. 17(a,b). As a result, the total sedi-  
 728    ment transport increases when considering the seepage response in Fig. 17(c),  
 729    which confirms the observation of Tonkin et al. (2003) and expectation of Yeh  
 730    and Mason (2014).

731    Fig. 18 illustrates the overall picture of the instantaneous suspended load  
 732    transport rate around the pile. At  $t/T = 0.25$ , the high suspended load  
 733    transport rate is mainly concentrated on the front side of the pile as seen in  
 734    Fig. 18(a,b) due to the combination of the horseshoe vortex and the stream-  
 735    line contraction. It spreads out downstream, which is less noticeable in  
 736    the presence of seabed suction for the simulated tsunami wave signal. At  
 737     $t/T = 0.75$ , the seabed injection increases the suspended load transport rate  
 738    around the circular pile. However, the momentary liquefaction does not occur  
 739    under the present tsunami and sediment conditions ( $i/i_c < 1$ , see Fig. 7a).

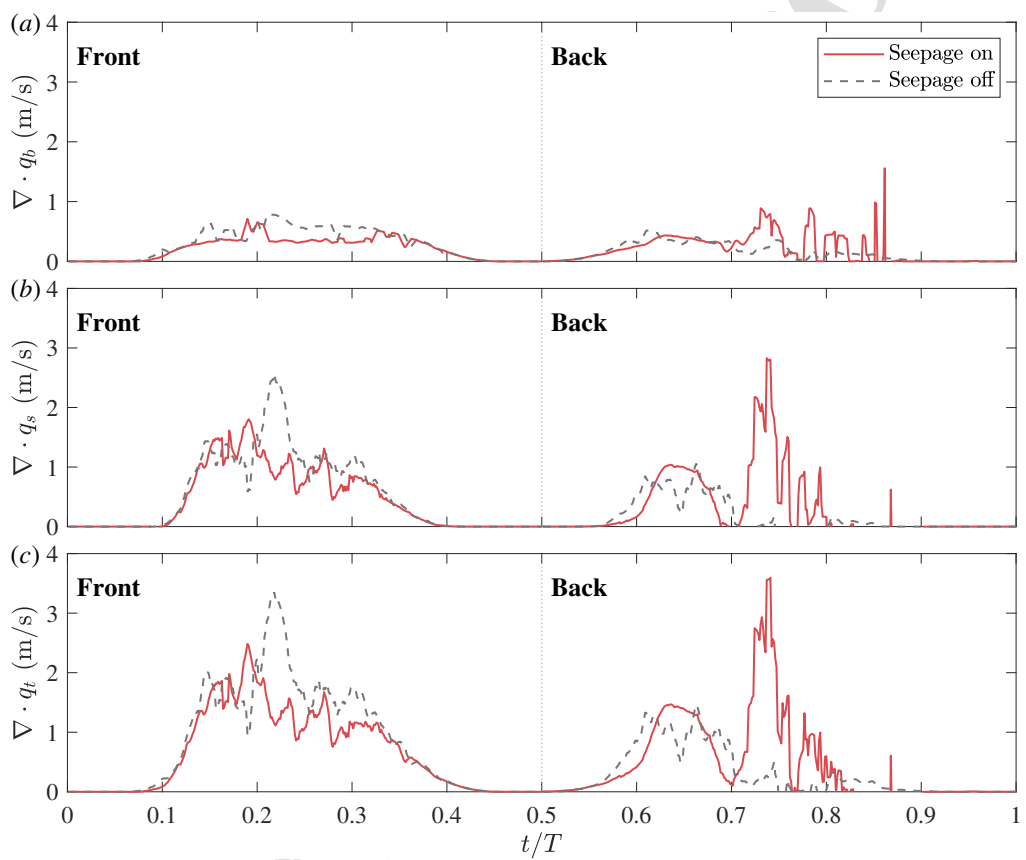


**Fig. 17.** Divergence of the (a) bed load transport rate  $q_b$ , (b) suspended load transport rate  $q_s$ , and (c) total load transport rate  $q_t$  at the front ( $t/T < 0.5$ ) and back ( $t/T > 0.5$ ) of the pile.

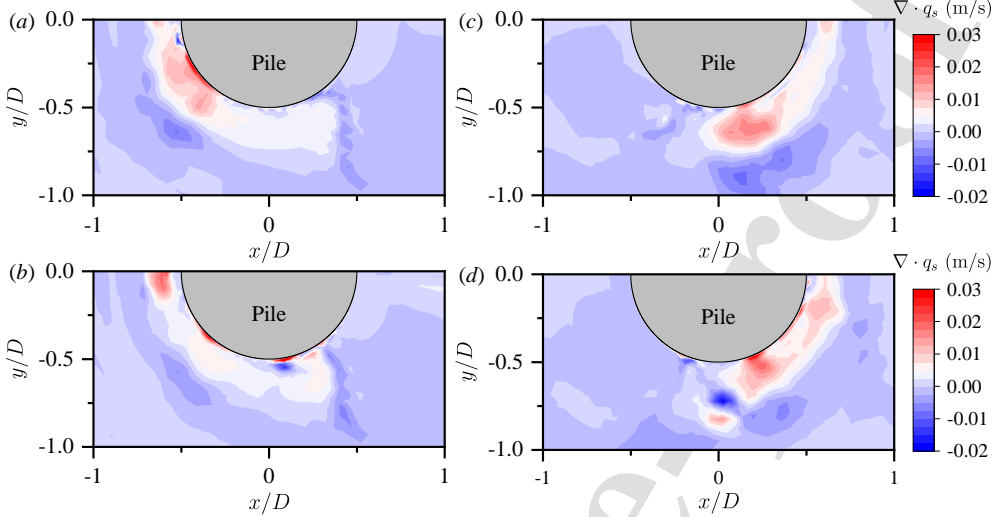


**Fig. 18.** Divergence of the suspended load transport rate around the circular pile (a,c) without and (b,d) with considering the seepage. The left panels are at  $t/T = 0.25$ , and the right panels are at  $t/T = 0.75$ .

## 740 6. Conclusions

741 In the present study, we have examined the role of seepage response in  
 742 full-scale tsunami-induced main flow features and scour around a circular  
 743 pile. The onset threshold of sediment transport and the bed load trans-  
 744 portation considering both bed-slope modifications and three-dimensional  
 745 seepage forces are analyzed and implemented in the coupled hydrodynamic,  
 746 morphological, and soil models. The main conclusions are drawn as follows:

747 In the rigid-bed simulations, we found that the seepage response can af-  
 748 fect the main tsunami flow features in the presence of a circular pile, which  
 749 determines the scour processes. The tsunami-induced vortical structures and  
 750 bed shear stress amplification around the pile resemble the intermediate be-  
 751 tween wind-generated waves and a steady current. Seabed suction during  
 752 the elevation wave can reduce the amplification of bed shear stress beneath  
 753 the contracted streamlines alongside the pile and lee-wake vortices. In con-  
 754 trast, seabed injection during the depression wave increases the shear stress  
 755 amplification. It advances the boundary layer separation point along the  
 756 pile height, further altering the lee-wake vortices. The size of the horseshoe  
 757 vortex and the upward-directed pressure gradient within it are minimally

758 impacted by the seepage flows.

759 In the morphological simulations, our results suggest that the suspended  
 760 sediment transport dominates the scour under full-scale tsunami waves. Seabed  
 761 suction during the elevation wave can slightly reduce the sediment transport  
 762 rate, decreasing the scour depth, especially at the pile side. Seabed injection  
 763 during the depression wave does cause a more rapid and severe scour at the  
 764 back of the pile, which is mainly due to the intensified suspended load trans-  
 765 port. If only the bed load transport is considered, the effect of seepage on  
 766 scour depth may not be obvious.

767 Our findings suggest that the seepage response should be considered when  
 768 assessing full-scale tsunami-induced scour around a circular pile. The present  
 769 model has several limitations. First, it does not account for the variability of  
 770 the wave surface, which may not capture the full complexity of fluid dynamics  
 771 affected by nearby structures during tsunami events. Additionally, the model  
 772 assumes that soil properties remain constant throughout the scour simula-  
 773 tions, overlooking potential changes due to dynamic loading. Future studies  
 774 will incorporate the effects of momentary liquefaction to better understand  
 775 severe tsunami-induced scour processes.

## 776 Acknowledgment

777 This research is supported by the Ministry of Education, Singapore, un-  
 778 der the Academic Research Fund Tier 1 (FY2021). This study is partly sup-  
 779 ported by computational resources provided by the National Supercomputing  
 780 Centre, Singapore (<https://www.nscc.sg>), under Project ID: 11002459.

## References

- Apotsos, A., Gelfenbaum, G., Jaffe, B., 2011. Process-based modeling of tsunami inundation and sediment transport. *J. Geophys. Res. Earth Surf.* 116. <https://doi.org/10.1029/2010JF001797>.
- Baker, C.J., 1979. The laminar horseshoe vortex. *J. Fluid Mech.* 95, 347–367. <https://doi.org/10.1017/S0022112079001506>.
- Baykal, C., Sumer, B.M., Fuhrman, D.R., Jacobsen, N.G., Fredsøe, J., 2015. Numerical investigation of flow and scour around a vertical circular cylinder. *Phil. Trans. R. Soc. A* 373, 20140104. <https://doi.org/10.1098/rsta.2014.0104>.

- Baykal, C., Sumer, B.M., Fuhrman, D.R., Jacobsen, N.G., Fredsøe, J., 2017. Numerical simulation of scour and backfilling processes around a circular pile in waves. *Coast. Eng.* 122, 87–107. <https://doi.org/10.1016/j.coastaleng.2017.01.004>.
- Biot, M.A., 1941. General theory of three-dimensional consolidation. *J. Appl. Phys.* 12, 155–164. <https://doi.org/10.1063/1.1712886>.
- Borrero, J.C., Cronin, S.J., Latu’ila, F.H., Tukuafu, P., Heni, N., Tupou, A.M., Kula, T., Fa’anunu, O., Bosserelle, C., Lane, E., Lynett, P., Kong, L., 2023. Tsunami runup and inundation in Tonga from the January 2022 eruption of Hunga volcano. *Pure Appl. Geophys.* 180, 1–22. <https://doi.org/10.1007/s00024-022-03215-5>.
- Bricker, J.D., Francis, M., Nakayama, A., 2012. Scour depths near coastal structures due to the 2011 Tohoku Tsunami. *J. Hydraul. Res.* 50, 637–641. <https://doi.org/10.1080/00221686.2012.721015>.
- Carrier, G.F., Wu, T.T., Yeh, H., 2003. Tsunami run-up and draw-down on a plane beach. *J. Fluid Mech.* 475, 79–99. <https://doi.org/10.1017/S0022112002002653>.
- Cebeci, T., Chang, K.C., 1978. Calculation of incompressible rough-wall boundary-layer flows. *AIAA J.* 16, 730–735. <https://doi.org/10.2514/3.7571>.
- Chan, I.C., Liu, P.L.F., 2012. On the runup of long waves on a plane beach. *J. Geophys. Res. Oceans* 117. <https://doi.org/10.1029/2012JC007994>.
- Chen, B., Li, S., 2018. Experimental study of local scour around a vertical cylinder under wave-only and combined wave-current conditions in a large-scale flume. *J. Hydraul. Eng.* 144, 04018058. [https://doi.org/10.1061/\(ASCE\)HY.1943-7900.0001502](https://doi.org/10.1061/(ASCE)HY.1943-7900.0001502).
- Chen, J., Huang, Z., Jiang, C., Deng, B., Long, Y., 2013. Tsunami-induced scour at coastal roadways: a laboratory study. *Nat Hazards* 69, 655–674. <https://doi.org/10.1007/s11069-013-0727-6>.
- Chen, S.g., Gong, E.y., Zhao, X., Arikawa, T., Chen, X., 2022. Large-scale experimental study on scour around offshore wind

- monopiles under irregular waves. *Water Sci. Eng.* 15, 40–46. <https://doi.org/10.1016/j.wse.2021.12.003>.
- Chen, X., Chiew, Y.M., 2004. Velocity distribution of turbulent open-channel flow with bed suction. *J. Hydraul. Eng.* 130, 140–148. [https://doi.org/10.1061/\(ASCE\)0733-9429\(2004\)130:2\(140\)](https://doi.org/10.1061/(ASCE)0733-9429(2004)130:2(140)).
- Cheng, N.S., Chiew, Y.M., 1998. Modified logarithmic law for velocity distribution subjected to upward seepage. *J. Hydraul. Eng.* 124, 1235–1241. [https://doi.org/10.1061/\(ASCE\)0733-9429\(1998\)124:12\(1235\)](https://doi.org/10.1061/(ASCE)0733-9429(1998)124:12(1235)).
- Cheng, N.S., Chiew, Y.M., 1999. Incipient sediment motion with upward seepage. *J. Hydraul. Res.* 37, 665–681. <https://doi.org/10.1080/00221689909498522>.
- Dawson, A.G., Shi, S., 2000. Tsunami deposits. *Pure Appl. Geophys.* 157, 875–897. [10.1007/s000240050010](https://doi.org/10.1007/s000240050010).
- Dey, S., Nath, T.K., 2010. Turbulence characteristics in flows subjected to boundary injection and suction. *J. Eng. Mech.* 136, 877–888. [https://doi.org/10.1061/\(ASCE\)EM.1943-7889.0000124](https://doi.org/10.1061/(ASCE)EM.1943-7889.0000124).
- Engelund, F., Fredsøe, J., 1976. A sediment transport model for straight alluvial channels. *Hydrol. Res.* 7, 293–306. <https://doi.org/10.2166/nh.1976.0019>.
- Fernandez Luque, R., Van Beek, R., 1976. Erosion and transport of bed-load sediment. *J. Hydraul. Res.* 14, 127–144. <https://doi.org/10.1080/00221687609499677>.
- Fredsøe, J., Deigaard, R., 1992. Mechanics of Coastal Sediment Transport. World Scientific, Singapore.
- Fritz, H.M., Kongko, W., Moore, A., McAdoo, B., Goff, J., Harbitz, C., Uslu, B., Kalligeris, N., Suteja, D., Kalsum, K., Titov, V., Gusman, A., Latief, H., Santoso, E., Sujoko, S., Djulkarnaen, D., Sunendar, H., Synolakis, C., 2007. Extreme runup from the 17 July 2006 Java tsunami. *Geophys. Res. Lett.* 34. <https://doi.org/10.1029/2007GL029404>.

- Fuhrman, D.R., Baykal, C., Sumer, B.M., Jacobsen, N.G., Fredsøe, J., 2014. Numerical simulation of wave-induced scour and backfilling processes beneath submarine pipelines. *Coast. Eng.* 94, 10–22. <https://doi.org/10.1016/j.coastaleng.2014.08.009>.
- Guan, D.w., Xie, Y.x., Yao, Z.s., Chiew, Y.M., Zhang, J.s., Zheng, J.h., 2022. Local scour at offshore windfarm monopile foundations: A review. *Water Sci. Eng.* 15, 29–39. <https://doi.org/10.1016/j.wse.2021.12.006>.
- Guo, Z., Jeng, D.S., Zhao, H., Guo, W., Wang, L., 2019. Effect of seepage flow on sediment incipient motion around a free spanning pipeline. *Coast. Eng.* 143, 50–62. <https://doi.org/10.1016/j.coastaleng.2018.10.012>.
- Gupta, B.K., Basu, D., 2020. Offshore wind turbine monopile foundations: Design perspectives. *Ocean Eng.* 213, 107514. <https://doi.org/10.1016/j.oceaneng.2020.107514>.
- Hjorth, P., 1975. Studies on the Nature of Local Scour. Lund Institute of Technology, University of Lund, Lund.
- Hu, Z., Huang, L., Li, Y., 2023. Fully-coupled hydroelastic modeling of a deformable wall in waves. *Coast. Eng.* 179, 104245. <https://doi.org/10.1016/j.coastaleng.2022.104245>.
- Hu, Z., Li, Y., 2023. Two-dimensional simulations of large-scale violent breaking wave impacts on a flexible wall. *Coast. Eng.* 185, 104370. <https://doi.org/10.1016/j.coastaleng.2023.104370>.
- Hu, Z., Qi, W.G., Li, Y., 2024. The role of dynamic seepage response in sediment transport and tsunami-induced scour. Submitted to *J. Geophys. Res. Oceans*.
- Hunt, J.C., Wray, A.A., Moin, P., 1988. Eddies, streams, and convergence zones in turbulent flows, in: Proceedings of the Summer Program 1988, Cent. Turbul. Res, Stanford, CA. p. 193–208.
- Issa, R.I., 1986. Solution of the implicitly discretised fluid flow equations by operator-splitting. *J. Comput. Phys.* 62, 40–65. [https://doi.org/10.1016/0021-9991\(86\)90099-9](https://doi.org/10.1016/0021-9991(86)90099-9).

- Jacobsen, N.G., 2011. A Full Hydro- and Morphodynamic Description of Breaker Bar Development. Ph.D. thesis. Technical University of Denmark.
- Jacobsen, N.G., Fredsøe, J., Jensen, J.H., 2014. Formation and development of a breaker bar under regular waves. Part 1: Model description and hydrodynamics. *Coast. Eng.* 88, 182–193. <https://doi.org/10.1016/j.coastaleng.2013.12.008>.
- Jayaratne, M.P.R., Premaratne, B., Adewale, A., Mikami, T., Matsuba, S., Shibayama, T., Esteban, M., Nistor, I., 2016. Failure mechanisms and local scour at coastal structures induced by tsunami. *Coast. Eng. J.* 58, 1640017. <https://doi.org/10.1016/10.1142/s0578563416400179>.
- Keulegan, G.H., Carpenter, L.H., 1958. Forces on cylinders and plates in an oscillating fluid. *J. Res. Natl. Bur. Stand.* 60, 423–440.
- Lacy, J.R., Rubin, D.M., Buscombe, D., 2012. Currents, drag, and sediment transport induced by a tsunami. *J. Geophys. Res. Oceans* 117. <https://doi.org/10.1029/2012JC007954>.
- Larsen, B.E., Arbøll, L.K., Kristoffersen, S.F., Carstensen, S., Fuhrman, D.R., 2018. Experimental study of tsunami-induced scour around a monopile foundation. *Coast. Eng.* 138, 9–21. <https://doi.org/10.1016/j.coastaleng.2018.04.007>.
- Larsen, B.E., Fuhrman, D.R., 2019a. Full-scale CFD simulation of tsunamis. Part 1: Model validation and run-up. *Coast. Eng.* 151, 22–41. <https://doi.org/10.1016/j.coastaleng.2019.04.012>.
- Larsen, B.E., Fuhrman, D.R., 2019b. Full-scale CFD simulation of tsunamis. Part 2: Boundary layers and bed shear stresses. *Coast. Eng.* 151, 42–57. <https://doi.org/10.1016/j.coastaleng.2019.04.011>.
- Larsen, B.E., Fuhrman, D.R., 2023. Re-parameterization of equilibrium scour depths and time scales for monopiles. *Coast. Eng.* 185, 104356. <https://doi.org/10.1016/j.coastaleng.2023.104356>.
- Larsen, B.E., Fuhrman, D.R., Baykal, C., Sumer, B.M., 2017. Tsunami-induced scour around monopile foundations. *Coast. Eng.* 129, 36–49. <https://doi.org/10.1016/j.coastaleng.2017.08.002>.

- Li, Y., Ong, M.C., Fuhrman, D.R., 2020a. CFD investigations of scour beneath a submarine pipeline with the effect of upward seepage. *Coast. Eng.* 156, 103624. <https://doi.org/10.1016/j.coastaleng.2019.103624>.
- Li, Y., Ong, M.C., Fuhrman, D.R., Larsen, B.E., 2020b. Numerical investigation of wave-plus-current induced scour beneath two submarine pipelines in tandem. *Coast. Eng.* 156, 103619. <https://doi.org/10.1016/j.coastaleng.2019.103619>.
- Li, Y., Ong, M.C., Tang, T., 2018. Numerical analysis of wave-induced poro-elastic seabed response around a hexagonal gravity-based offshore foundation. *Coast. Eng.* 136, 81–95. <https://doi.org/10.1016/j.coastaleng.2018.02.005>.
- Li, Y., Ong, M.C., Tang, T., 2020c. A numerical toolbox for wave-induced seabed response analysis around marine structures in the OpenFOAM® framework. *Ocean Eng.* 195, 106678. <https://doi.org/10.1016/j.oceaneng.2019.106678>.
- Liu, P.L.F., Higuera, P., 2022. Water waves generated by moving atmospheric pressure: theoretical analyses with applications to the 2022 Tonga event. *J. Fluid Mech.* 951, A34. <https://doi.org/10.1016/10.1017/jfm.2022.840>.
- Liu, P.L.F., Park, Y.S., Lara, J.L., 2007. Long-wave-induced flows in an unsaturated permeable seabed. *J. Fluid Mech.* 586, 323–345. <https://doi.org/10.1017/S0022112007007057>.
- Lynett, P., McCann, M., Zhou, Z., Renteria, W., Borrero, J., Greer, D., Fa'anunu, O., Bosserelle, C., Jaffe, B., La Selle, S., Ritchie, A., Snyder, A., Nasr, B., Bott, J., Graehl, N., Synolakis, C., Ebrahimi, B., Cinar, G.E., 2022. Diverse tsunamigenesis triggered by the Hunga Tonga-Hunga Ha'apai eruption. *Nature* 609, 728–733. [10.1038/s41586-022-05170-6](https://doi.org/10.1038/s41586-022-05170-6).
- Madsen, P.A., Fuhrman, D.R., Schäffer, H.A., 2008. On the solitary wave paradigm for tsunamis. *J. Geophys. Res. Oceans* 113. <https://doi.org/10.1029/2008JC004932>.
- McGovern, D.J., Todd, D., Rossetto, T., Whitehouse, R.J.S., Monaghan, J., Gomes, E., 2019. Experimental observations of tsunami induced scour at onshore structures. *Coast. Eng.* 152, 103505. <https://doi.org/10.1016/j.coastaleng.2019.103505>.

- Mori, N., Takahashi, T., Yasuda, T., Yanagisawa, H., 2011. Survey of 2011 Tohoku earthquake tsunami inundation and run-up. *Geophys. Res. Lett.* 38. <https://doi.org/10.1029/2011GL049210>.
- Nakamura, T., Kuramitsu, Y., Mizutani, N., 2008. Tsunami scour around a square structure. *Coast. Eng. J.* 50, 209–246. <https://doi.org/10.1142/S057856340800179X>.
- Omira, R., Ramalho, R.S., Kim, J., González, P.J., Kadri, U., Miranda, J.M., Carrilho, F., Baptista, M.A., 2022. Global Tonga tsunami explained by a fast-moving atmospheric source. *Nature* 609, 734–740. 10.1038/s41586-022-04926-4.
- Patankar, S.V., Spalding, D.B., 1972. A calculation procedure for heat, mass and momentum transfer in three-dimensional parabolic flows. *Int. J. Heat Mass Transf.* 15, 1787–1806. [https://doi.org/10.1016/0017-9310\(72\)90054-3](https://doi.org/10.1016/0017-9310(72)90054-3).
- Qi, W.G., Gao, F.P., 2014. Physical modeling of local scour development around a large-diameter monopile in combined waves and current. *Coast. Eng.* 83, 72–81. <https://doi.org/10.1016/j.coastaleng.2013.10.007>.
- Qi, W.G., Gao, F.P., 2018. Wave induced instantaneously-liquefied soil depth in a non-cohesive seabed. *Ocean Eng.* 153, 412–423. <https://doi.org/10.1016/j.oceaneng.2018.01.107>.
- Ren, Z., Higuera, P., Liu, P.L.F., 2023. On tsunami waves induced by atmospheric pressure shock waves after the 2022 Hunga Tonga-Hunga Ha'apai volcano eruption. *J. Geophys. Res. Oceans* 128, e2022JC019166. <https://doi.org/10.1029/2022JC019166>.
- Robbe-Saule, M., Morize, C., Henaff, R., Bertho, Y., Sauret, A., Gondret, P., 2021. Experimental investigation of tsunami waves generated by granular collapse into water. *J. Fluid Mech.* 907, A11. <https://doi.org/10.1016/10.1017/jfm.2020.807>.
- Roulund, A., Sumer, B.M., Fredsøe, J., Michelsen, J., 2005. Numerical and experimental investigation of flow and scour around a circular pile. *J. Fluid Mech.* 534, 351–401. <https://doi.org/10.1017/S0022112005004507>.

- Sarlin, W., Morize, C., Sauret, A., Gondret, P., 2021. Nonlinear regimes of tsunami waves generated by a granular collapse. *J. Fluid Mech.* 919, R6. <https://doi.org/10.1016/10.1017/jfm.2021.400>.
- Satake, K., Bourgeois, J., Abe, K., Abe, K., Tsuji, Y., Imamura, F., Lio, Y., Katao, H., Noguera, E., Estrada, F., 1993. Tsunami field survey of the 1992 Nicaragua earthquake. *Eos, Transactions American Geophysical Union* 74, 145–157. <https://doi.org/10.1029/93EO00271>.
- Sharma, A., Kumar, B., 2017. Structure of turbulence over non uniform sand bed channel with downward seepage. *Eur. J. Mech. B/Fluids.* 65, 530–551. <https://doi.org/10.1016/j.euromechflu.2017.05.006>.
- Sugawara, D., Goto, K., Jaffe, B.E., 2014. Numerical models of tsunami sediment transport — current understanding and future directions. *Mar. Geol.* 352, 295–320. <https://doi.org/10.1016/j.margeo.2014.02.007>.
- Sui, T., Liu, C., Zhang, J., Zhang, C., Zheng, J., 2024. 3D numerical modeling of wave-monopile-seabed interaction in the presence of a scour hole. *Ocean Eng.* 298, 117254. <https://doi.org/10.1016/j.oceaneng.2024.117254>.
- Sui, T., Staunstrup, L.H., Carstensen, S., Fuhrman, D.R., 2021. Span shoulder migration in three-dimensional current-induced scour beneath submerged pipelines. *Coast. Eng.* 164, 103776. <https://doi.org/10.1016/j.coastaleng.2020.103776>.
- Sumer, B.M., 2006. Hydrodynamics around Cylindrical Strucures. World scientific.
- Sumer, B.M., 2014. Liquefaction Around Marine Structures. World Scientific. <https://doi.org/10.1142/7986>.
- Sumer, B.M., Christiansen, N., Fredsøe, J., 1997. The horseshoe vortex and vortex shedding around a vertical wall-mounted cylinder exposed to waves. *J. Fluid Mech.* 332, 41–70. <https://doi.org/10.1017/S0022112096003898>.
- Sumer, B.M., Fredsøe, J., 2001. Scour around pile in combined waves and current. *J. Hydraul. Eng.* 127, 403–411. [https://doi.org/10.1061/\(ASCE\)0733-9429\(2001\)127:5\(403\)](https://doi.org/10.1061/(ASCE)0733-9429(2001)127:5(403)).

- Sumer, B.M., Fredsøe, J., 2002. The Mechanics of Scour in the Marine Environment. World Scientific.
- Sumer, B.M., Fredsøe, J., Christiansen, N., 1992. Scour around vertical pile in waves. *J. Waterw. Port, Coast. Ocean Eng.* 118, 15–31. [https://doi.org/10.1061/\(ASCE\)0733-950X\(1992\)118:1\(15\)](https://doi.org/10.1061/(ASCE)0733-950X(1992)118:1(15)).
- Sumer, B.M., Petersen, T.U., Locatelli, L., Fredsøe, J., Musumeci, R.E., Foti, E., 2013. Backfilling of a scour hole around a pile in waves and current. *J. Waterw. Port, Coast. Ocean Eng.* 139, 9–23. [https://doi.org/10.1061/\(ASCE\)WW.1943-5460.0000161](https://doi.org/10.1061/(ASCE)WW.1943-5460.0000161).
- Taye, J., Sharma, A., Kumar, B., 2023. Effect of downward seepage on turbulence and morphology in mobile boundary sinuous channel. *Phys. Fluids* 35. <https://doi.org/10.1063/5.0133201>.
- Tong, L., Liu, P.L.F., 2022. Transient wave-induced pore-water-pressure and soil responses in a shallow unsaturated poroelastic seabed. *J. Fluid Mech.* 938, A36. <https://doi.org/10.1017/jfm.2022.184>.
- Tonkin, S., Yeh, H., Kato, F., Sato, S., 2003. Tsunami scour around a cylinder. *J. Fluid Mech.* 496, 165–192. <https://doi.org/10.1017/S0022112003006402>.
- Van Driest, E.R., 1956. On turbulent flow near a wall. *J. aeronaut. sci.* 23, 1007–1011. <https://doi.org/10.2514/8.3713>.
- Wang, Z., Pan, J., Xie, D., Zhang, C., Sui, T., 2024. Influence of cnoidal wave-induced seepage force on shields number in shallow water. *Ocean Eng.* 310, 118690. <https://doi.org/10.1016/j.oceaneng.2024.118690>.
- Whitehouse, R.J.S., Stroescu, E.I., 2023. Scour depth development at piles of different height under the action of cyclic (tidal) flow. *Coast. Eng.* 179, 104225. <https://doi.org/10.1016/j.coastaleng.2022.104225>.
- Wilcox, D.C., 2006. Turbulence Modeling for CFD. 3rd ed., DCW Industries.
- Wilcox, D.C., 2008. Formulation of the  $k-\omega$  turbulence model revisited. *AIAA J.* 46, 2823–2838. <https://doi.org/10.2514/1.36541>.

- Williams, I.A., Fuhrman, D.R., 2016. Numerical simulation of tsunami-scale wave boundary layers. *Coast. Eng.* 110, 17–31. <https://doi.org/10.1016/j.coastaleng.2015.12.002>.
- Wilson, R., Davenport, C., Jaffe, B., 2012. Sediment scour and deposition within harbors in California (USA), caused by the March 11, 2011 Tohoku-oki tsunami. *Sediment. Geol.* 282, 228–240. <https://doi.org/10.1016/j.sedgeo.2012.06.001>.
- Ye, J., Zhou, H., He, K., 2024. A generalized framework of two-way coupled numerical model for fluid-structure-seabed interaction (FSSI): Explicit algorithm. *Eng. Geol.* 340, 107679. <https://doi.org/10.1016/j.enggeo.2024.107679>.
- Yeh, H., Mason, H., 2014. Sediment response to tsunami loading: mechanisms and estimates. *Géotechnique* 64, 131–143. <https://doi.org/10.1680/geot.13.P.033>.
- Yeh, H., Sato, S., Tajima, Y., 2013. The 11 March 2011 East Japan earthquake and tsunami: Tsunami effects on coastal infrastructure and buildings. *Pure Appl. Geophys.* 170, 1019–1031. <https://doi.org/10.1007/s00024-012-0489-1>.
- Yoshii, T., Tanaka, S., Matsuyama, M., 2017. Tsunami deposits in a super-large wave flume. *Mar. Geol.* 391, 98–107. <https://doi.org/10.1016/j.margeo.2017.07.020>.
- Yoshii, T., Tanaka, S., Matsuyama, M., 2018. Tsunami inundation, sediment transport, and deposition process of tsunami deposits on coastal lowland inferred from the Tsunami Sand Transport Laboratory Experiment (TSTLE). *Mar. Geol.* 400, 107–118. <https://doi.org/10.1016/j.margeo.2018.03.007>.
- Zhai, H., Jeng, D.S., 2022. Two-way coupling model for wave-induced oscillatory soil response around marine structures. *Ocean Eng.* 249, 110791. <https://doi.org/10.1016/j.oceaneng.2022.110791>.
- Zhai, H., Jeng, D.S., 2024. Impacts of wave-induced seabed response on local scour around a pipeline: POREO–FSSI–SCOUR–FOAM. *Coast. Eng.* 187, 104424. <https://doi.org/10.1016/j.coastaleng.2023.104424>.

- Zhai, H., Jeng, D.S., Guo, Z., Liang, Z., 2021a. Impact of two-dimensional seepage flow on sediment incipient motion under waves. *Appl. Ocean Res.* 108, 102510. <https://doi.org/10.1016/j.apor.2020.102510>.
- Zhai, H., Jeng, D.S., Guo, Z., Sui, T., 2021b. Modified Shields number for sediment incipient motion around a pile with impact of three-dimensional seepage in a porous seabed. *Appl. Ocean Res.* 117, 102896. <https://doi.org/10.1016/j.apor.2021.102896>.
- Zhang, S., Li, B., Ma, H., 2023. Numerical investigation of scour around the monopile using CFD-DEM coupling method. *Coast. Eng.* 183, 104334. <https://doi.org/10.1016/j.coastaleng.2023.104334>.
- Zhao, M., Cheng, L., 2008. Numerical modeling of local scour below a piggyback pipeline in currents. *J. Hydraul. Eng.* 134, 1452–1463. [https://doi.org/10.1061/\(ASCE\)0733-9429\(2008\)134:10\(1452\)](https://doi.org/10.1061/(ASCE)0733-9429(2008)134:10(1452)).
- Zhao, M., Cheng, L., Zang, Z., 2010. Experimental and numerical investigation of local scour around a submerged vertical circular cylinder in steady currents. *Coast. Eng.* 57, 709–721. <https://doi.org/10.1016/j.coastaleng.2010.03.002>.
- Zou, X., Cao, X., Zhou, C., Zhou, M., Zhang, X., 2021. Experimental study on the bearing capacity of large-diameter monopile in sand under water flow condition. *Ocean Eng.* 224, 108708. <https://doi.org/10.1016/j.oceaneng.2021.108708>.

## Highlights

### **Full-scale tsunami-induced scour around a circular pile with three-dimensional seepage**

Zhengyu Hu, Yuzhu Pearl Li

- The role of seepage response in full-scale tsunami scour around a circular pile is studied
- The incipient sediment motion and bed load transport are analyzed considering bed-slope modification and three-dimensional seepage
- The hydrodynamic, morphological, and soil models are coupled in the finite volume framework
- Tsunami-induced flow features and morphological evolution around a pile are presented with and without considering seepage effects

**Declaration of interests**

The authors declare that they have no known competing financial interests or personal relationships that could have appeared to influence the work reported in this paper.

The authors declare the following financial interests/personal relationships which may be considered as potential competing interests:

